

# JGR Earth Surface

## RESEARCH ARTICLE

10.1029/2021JF006355

### Key Points:

- Agricultural irrigation triggers widespread landslides in a Washington desert valley
- Forced water circulation on irregular slip surface can explain early landslide deceleration
- Slip surface steepness bifurcates slow and catastrophic landslide movements

### Correspondence to:

Y. Xu,  
[yuankunx@berkeley.edu](mailto:yuankunx@berkeley.edu)

### Citation:

Xu, Y., Lu, Z., & Leshchinsky, B. (2022). Kinematics of irrigation-induced landslides in a Washington desert: Impacts of basal geometry. *Journal of Geophysical Research: Earth Surface*, 127, e2021JF006355. <https://doi.org/10.1029/2021JF006355>

Received 21 JUL 2021  
Accepted 28 JAN 2022

## Kinematics of Irrigation-Induced Landslides in a Washington Desert: Impacts of Basal Geometry

Yuankun Xu<sup>1,2</sup> , Zhong Lu<sup>1</sup> , and Ben Leshchinsky<sup>3</sup> 

<sup>1</sup>Roy M. Huffington Department of Earth Sciences, Southern Methodist University, Dallas, TX, USA, <sup>2</sup>Department of Earth and Planetary Science, University of California, Berkeley, Berkeley, CA, USA, <sup>3</sup>School of Civil and Construction Engineering, College of Forestry, Oregon State University, Corvallis, OR, USA

**Abstract** Landslides are often considered to be a natural hazard that frequently occurs in mountainous, precipitation-abundant regions worldwide; however, they can also occur in dry climates resulting from anthropogenic influences, such as irrigation farming. Generally less affected by precipitation, landslides in arid regions are ideal for examining impacts of non-precipitation controls on landslide motion, such as basal geometry. Here, we focused on 25 large, irrigation-triggered, slow-moving and catastrophic landslides that occurred in a desert valley near Hanford, Washington along the Columbia River. Optical images in submeter resolution from 1996 to 2020 and Sentinel-1 interferometric synthetic aperture radar (InSAR) deformation measurements from 2016 to 2020 were utilized to map 12 catastrophic landslides and obtain time-series deformation of 13 actively slow-moving landslide complexes. Our results show that the catastrophic landslides usually completed their life cycle from initiation to final deposition within minutes to days, whereas the slow-moving ones have lasted approximately 40 years, exhibiting rapid acceleration and a subsequent deceleration period that is almost 12 times longer. Though varying in rates, both types of landslides facilitate sediment transport into the Columbia River, which is of concern for aquatic habitats. Motion dynamics of the four riverside, slow-moving landslides were strongly modulated by the Columbia River height subject to seasonal dam water release, whereas the eight river-distant landslides primarily respond to the infiltrated irrigation water from the farmlands. We observed an apparent “early deceleration” phenomenon for the riverside Locke landslide, where the landslide starts to decelerate despite the threshold groundwater conditions being exceeded. We interpret that the early decelerations result from the forced water circulation near the basal-surface asperities, because river bathymetry data suggest that basal surfaces of the Locke landslide (originally the Columbia River bed) are highly irregular. This interpretation was also supported by numerical simulations, which show that incorporating the forced water circulation may help accurately predict the InSAR-observed maximum velocity and the timing of deceleration. Additionally, our analyses of basal profiles of 10 slow-moving and catastrophic landslides in the study region reveal that basal geometry could impart a bifurcation between slow and catastrophic landslide movements. Gentle basal surfaces are more likely associated with large, slow-moving landslides, whereas steep ones are often involved with relatively small, catastrophic landslides due to rapid kinetic energy gains while moving downslope. In general, the examined impacts of basal geometry in this study are widely applicable to natural landslides worldwide for their kinematics characterization and forecasting.

**Plain Language Summary** Landslides in arid regions are barely affected by ground rainfall and therefore provide a unique opportunity to study how other factors, such as slip surface geometry, affect landslide motion dynamics. In this study, we used Google Earth optical images and Sentinel-1 radar images to measure deformation of 25 landslides in a desert valley near Hanford, Washington. Our results show that the riverside landslides are strongly impacted by the river water level, which is controlled by an upstream dam. Interestingly, an early deceleration phenomenon was captured for the riverside Locke landslide, where the slide starts to decelerate while the groundwater level remains above the threshold that initially triggered the seasonal slide acceleration. The inferred slip surface and numerical simulations suggest that the observed early decelerations can be explained by the forced water circulation on an irregular sliding surface during landslide movement. We also found that the steepness of basal surface could cause a bifurcation of slow and catastrophic landslide movements. Steep basal surfaces are more likely to cause catastrophic landslide rather than a slow-moving one. Our findings of the basal surface's impacts on landslide movement are critical for forecasting landslide motions and are widely applicable to many similar slides worldwide.

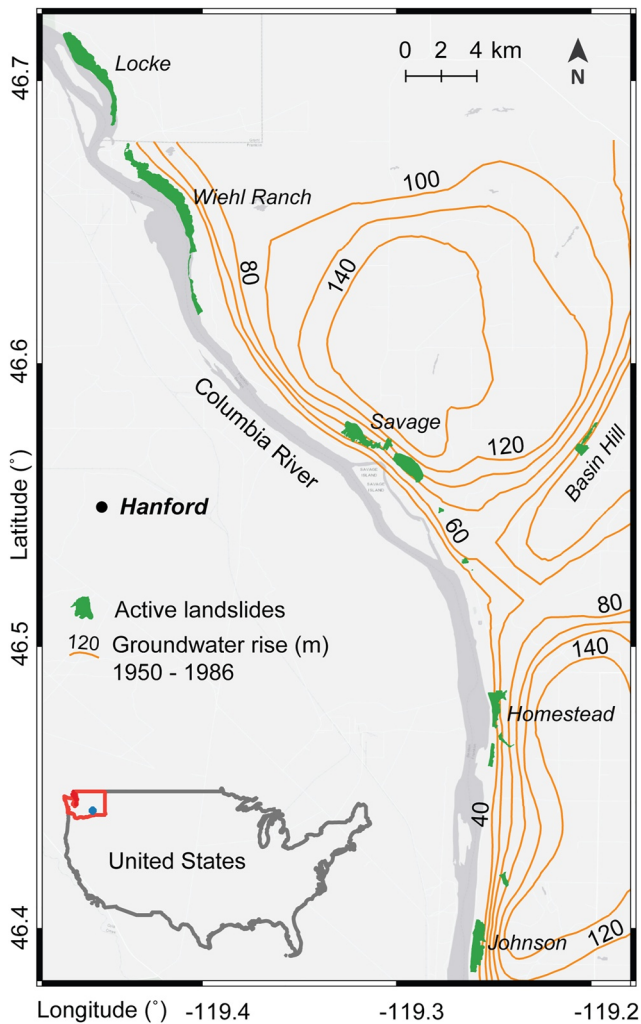


**Figure 1.** Geographical location of the study area near Hanford, Washington. A scaled-down map is shown at the bottom-left corner. The groundwater level data were modified from Drost et al., 1993.

## 1. Introduction

Landslides are a natural, gravity-driven geomorphic process that transports unstable materials downslope and modifies landscapes during both short and long timescales depending on their rate of motion (Highland & Bobrowsky, 2008; Mackey & Roering, 2011; Simoni et al., 2013). As a frequent natural hazard, landslides claim thousands of human lives and cause billion dollars of property loss on a global basis annually (Froude & Petley, 2018; Spiker & Gori, 2003). Common natural triggers of landslides include intense precipitation, earthquakes, and erosive processes (Highland & Bobrowsky, 2008); however, anthropogenic activities are becoming an increasingly frequent trigger for slope failures in the recent decades (Froude & Petley, 2018). Especially, agricultural irrigation has become one of the common triggers for many large landslides, particularly in arid and semiarid regions around the world where irrigation is a requisite for farming (see a review by Garcia-Chevesich et al. (2021)). Monitoring irrigation-triggered landslides could help evaluate how irrigation impacts slope stability and provides insights for reducing these landslide hazards.

The evolution of landslide motion after initiation significantly affects their hazard level. Slow-moving landslides consistently damage infrastructure in their vicinity, whereas catastrophic runout landslides pose escalated hazards to both infrastructure and human lives over extended spatial extents (e.g., Highland & Bobrowsky, 2008; Xu, George, et al., 2021). For example, landslide-initiated debris flows may travel several kilometers downstream/downslope with little warning, posing serious risk to life safety (Legros, 2002). Deciphering the mechanisms that modulate post-initiation kinematics of landslides is critical for understanding and mitigating their hazards. Multiple hydrogeological factors, such as rainfall infiltration (Iverson, 2000), dilation and contraction of shear-zone material (Casagrande, 1976), and uneven slip surface geometry (Baum & Johnson, 1993) could regulate landslide motion by altering basal pore pressure (Terzaghi, 1950). However, isolating and quantifying the contribution of each element have always been challenging owing to the complex nature of most natural landslides. In comparison to landslides in rainfall-abundant regions where precipitation strongly modulates landslide motion (e.g., Handwerger et al., 2013; Xu et al., 2019; Xu et al., 2020), landslides in arid climates (e.g., the Locke landslide in Figures 1 and 2b) are less affected by precipitation and therefore offer a unique opportunity to focus on other disturbances than surface water infiltration. To illustrate, the Locke

landslide was initiated by irrigation water diverted to a pond near the landslide in the 1960s, and the water pond was later manually drained in the mid-1990s (Bjornstad & Peterson, 2019). As the Locke landslide is also located in a desert environment where evaporation exceeds precipitation (Peel et al., 2007), its present motions are barely affected by surface precipitation. Consequently, such irrigation-induced landslides in a desert provide an ideal and natural laboratory setting for investigating contributing factors other than surface precipitation.

This investigation focuses on landslides triggered by agricultural irrigation in the desert near Hanford, Washington, United States. Satellite optical and radar images are used to identify both creeping and catastrophic landslides in the study region and to measure their post-initiation motion dynamics. Field photos and compiled soil laboratory tests data help to explain how excessive irrigation water led to widespread landslide activity along the desert valley in Hanford. The typical life cycles of both slow-moving landslides and catastrophic runout landslides from initiation to final deposition are characterized by capturing and integrating concurrent landslides in variable stages of their lives. Moreover, by incorporating groundwater and inferred basal geometry data for multiple landslides, the critical impacts of basal geometry on landslide post-initiation motion are evaluated from integrating satellite observations and numerical modeling.

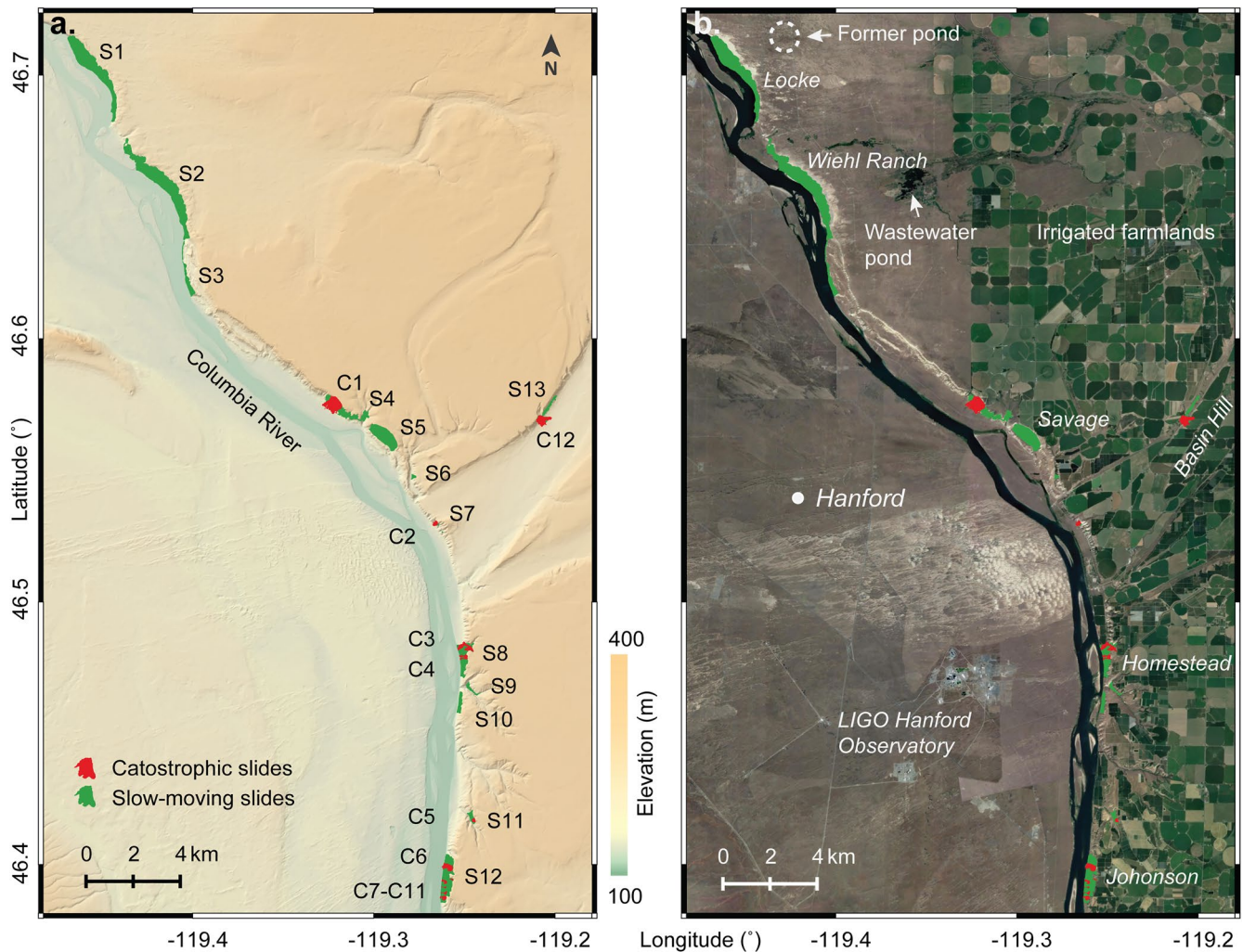


**Figure 2.** Irrigation-triggered landslides in a desert near Hanford, Washington. (a) S1–S13 denote the slow-moving landslides identified from SAR interferograms between 2015 and 2020. C1–C11 mark catastrophic landslides identified from Google Earth true color images. Some catastrophic landslides and slow-moving landslides may overlap. The background hillshade map was produced from the 10-m resolution National Elevation Datasets (USGS, 2021a). (b) A Google Earth true color image acquired in 2020 that covers the same geographical extent as (a). The irrigated farmlands are mostly in green color.

Our investigation provides insight into how agricultural irrigation destabilizes hillslopes, how groundwater level modulates landslide movement, and how basal geometry regulates landslide post-initiation kinematics. This knowledge can be widely applied to not only irrigation-triggered landslides but also many natural hillslope failures worldwide for landslide hazard reduction.

## 2. Irrigation-Triggered Desert Landslides Near Hanford

Hanford is located in south-central Washington state and is categorized as a cold desert climate (Peel et al., 2007) where evaporation exceeds precipitation. This region receives an annual rainfall of ~180 mm/year (Figure 1), 15% of which is in the form of snow. The annual evaporation rate averages 213 mm/year from 2003 to 2019 (Martens et al., 2017). Prior to 1950, the arid lands near Hanford were dominated by dryland farming (Schuster et al., 1989). Since 1950, continuous development of the Columbia Basin Project has transformed this region into one of the most productive agricultural areas in the United States (Drost, et al., 1993), primarily achieved by importing irrigation water from the upstream Columbia River through dams and canals. About 1500 mm of irrigation water (per m<sup>2</sup>) was diverted annually to the farmlands east of the Columbia River (Schuster et al., 1989,



Figure 1). However, such successful agricultural transformation had unforeseen consequences: widespread landslides were triggered along the desert valley near Hanford (Bjornstad & Peterson, 2019; Figure 1; Schuster et al., 1989), which have consequently damaged roads and houses and harmed salmon spawning in the nearby Columbia River through the transport of a considerable amount of sediment downstream (Drost, et al., 1993).

The eastern banks of the Columbia River in the study area are composed of steep bluffs, typically 45–170 m in height. Geologically, these bluffs are predominantly composed of the Ringold Formation, which overlays rocks of the Columbia River Basalt Group and is capped by Quaternary fluvial and windblown sediments (Schuster et al., 1989). The Ringold Formation is termed for the nearly horizontal, soft rock layers (locally dipped toward the Columbia River by approximately one degree), which are composed of weakly indurated claystone, siltstones, and sandstones near Hanford (Schuster et al., 1989). Mechanically, the strength of soft rocks of the Ringold Formation exhibits notable anisotropy and sensitivity to moisture: relatively strong when dry, yet the rocks weaken significantly when wetted. Laboratory tests of undisturbed soil samples from the bluff (Bareither et al., 2012) show that saturating the soil sample decreases the friction angle from 32.9° to 19.8° and the cohesion from 274 to 46 kPa in the vertical orientation. Along the horizontal orientation, it reduces the friction angle from 22.7° to 21° and the cohesion from 368 to 16.7 kPa.

From 1950 until March 1983, excessive agricultural irrigation resulted in the accretion of groundwater, where head levels in the study area rose by 40–140 m (Figure 1) from unlined canal leakage and wastewater drainage (Drost, et al., 1993). Low-permeability, fine-grained layers may have also resulted in perched groundwater conditions and preferential horizontal flow, suggested by seeps along nearby bluffs (Bjornstad & Peterson, 2019). A combination of elevated pore pressures and progressively weakening rocks/soils has contributed to a widespread landslide activity along the steep bluffs along the Columbia River and other hillslopes in the study region (Bjornstad & Peterson, 2019; Figure 1; Schuster et al., 1989). Six of these large landslide complexes, including the Locke landslide, the Wiehl Ranch landslide, the Savage landslide, the Homestead landslide, the Johnson landslide, and the Basin Hill landslide, are shown in Figure 1. Additionally, seasonal water release from an upstream dam appeared to directly impact the motion rates of riverside landslides by fluctuating basal pore pressure (see details in Section 4.2.2).

### 3. Data and Methods

This investigation aims at mapping active landslides and measuring their time-series surface displacements using satellite optical and radar images. The Interferometric Synthetic Aperture Radar (InSAR) technique was applied to the satellite radar images. Moreover, numerical modeling and topographical maps were incorporated to interpret mechanisms of the contrasting post-initiation slow and rapid motions of the observed landslides.

Following the landslide velocity scale defined in Cruden and Varnes (1996), we regrouped the landslide categories and termed the landslides spanning from extremely slow to moderate (less than  $5 \times 10^{-3}$  mm/s) as slow-moving landslides, and the ones ranging from rapid to extremely rapid ( $5 \times 10^{-1}$ – $5 \times 10^3$  mm/s) as catastrophic landslides in this study. The slow-moving landslides were determined from InSAR measurements, whereas the catastrophic failures usually lacked real-time speed measurements and were primarily inferred from their characteristic long runout paths on satellite optical images.

#### 3.1. Data

The Sentinel-1 SAR images from the ascending track A166 (January 2016–September 2020) and the descending track D42 (August 2015–September 2020) were used to detect slow-moving landslides and measure their time-series displacements. Google Earth images with submeter and 1-m resolutions from 1996 to 2020 were utilized to identify catastrophic landslides and measure time-series motion of a relatively fast landslide. The 1965 topographical map, the 10-m-resolution National Elevation Datasets (USGS, 2021a), and the approximately 1-m-resolution 2010 surface DEMs and river bathymetry data from Washington Department of Natural Resources (DNR) were employed to produce pre-landslide and/or post-landslide topography of selected landslides.

Daily water level and discharge rate of the Columbia River were obtained from a river gauge (USGS 12472800; USGS, 2021b) located 4.2 km below the Priest Rapids Dam and 38 km upstream of the Locke landslide

(Figure 2). The water level and discharge rate average 4.65 m and 3,324.6 m<sup>3</sup>/s, respectively, between 1992 and 2020 (USGS, 2021b). Based on the cross-section area measured from the 2010 surface DEM and the 2010 river bathymetry, the average flow velocity near the gauging station is approximately 3.08 m/s, indicating that the water flows from the gauge station to the Locke landslide in approximately 3.4 hr. Daily precipitation data of the study area were obtained from a meteorological station at the Saddle Mountain (18 km west of the Locke landslide in Figure 2b; WRCC, 2021). Groundwater records from 1964 to 1983 were collected at a well 1 km east of the Johnson landslide by U.S. Bureau of Reclamation (Figure 2b; Schuster et al., 1989). Annual evaporation rates of the Hanford region (i.e., 213 mm/year during 2003–2019 and 243 mm/year during 2016–2019) were obtained from the satellite-based GLEAM data with a spatial resolution of 0.25° × 0.25° (Martens et al., 2017).

### 3.2. InSAR Measurements

#### 3.2.1. Multitemporal InSAR Processing

SAR interferometry is a technique that utilizes the phase information in satellite radar images to achieve displacement measurement of ground objects in optimally millimeter-level accuracy (e.g., Ferretti et al., 2007). A SAR interferogram is produced from interferometry of two repeat-path SAR images that are usually separated by several days or weeks. Multiple SAR interferograms spanning varied observation periods can be used to generate time-series measurements of a ground target.

In this investigation, we utilized both ascending and descending Sentinel-1 SAR images from 2015 to 2020 to obtain InSAR time-series measurement of the target slow-moving landslides. The National Elevation Datasets (USGS, 2021a) covering the study area were used to remove topography-contributed InSAR phase during SAR interferogram generation. The Sentinel-1 SAR images were multi-looked using factors of 5 × 2 (range by azimuth) to a pixel size of 12 × 28 m during interferometric processing, and the generated interferograms were unwrapped with the minimum cost flow method (Costantini, 1998) before a geocoding process using the 10-m-resolution DEMs. The coherence threshold was set to 0.4 for the phase unwrapping. Stratified tropospheric artifacts associated with surface topography were removed after phase unwrapping. Stable, high-coherence (coherence > 0.7) reference regions (300 × 300 m) within 1 km distance from each target landslide were selected to remove potential artifacts sourcing from regional soil moisture changes and turbulent troposphere in the interferograms.

Multitemporal InSAR processing was achieved by using a coherence-weighted small baseline subset (SBAS) method (see details in Xu et al., 2020). We selected only interferograms spanning the two closest dates for the time-series inversion and therefore, each utilized SAR interferogram is indispensable and completely independent in the time domain for the time-series measurements. Based on statistics of multiple manually selected stable areas (within 1 km to the reference regions) in the study region, the measurement accuracy of relatively coherent points (coherence ≥ 0.4) of a single SAR interferogram was within 4 mm (i.e.,  $\sigma_s = 4$  mm), which was slightly lower than the submillimeter level achieved by using corner reflectors (Ferretti et al., 2007). The accuracy of time-series measurements for the  $n$ th date can be calculated as  $\sigma_{ts} = \sqrt{n} \cdot \sigma_s$ , following propagation of uncertainty. Hence, the cumulative uncertainty for the last time-series measurement (the 111th) during the observation period was 4.2 cm.

#### 3.2.2. LOS Measurements to Landslide Downslope Direction

In a three-dimensional geographical coordinate system, the unit vector of radar LOS direction can be decomposed as  $l = \begin{bmatrix} \sin \theta_{inc} \cos \phi_{head} & -\sin \theta_{inc} \sin \phi_{head} & -\cos \theta_{inc} \end{bmatrix}$  along the east, north, and zenith directions, where  $\theta_{inc}$  is the incidence angle of the right-looking SAR sensor and  $\phi_{head}$  is the heading angle of the satellite flying path (clockwise from north as positive). Similarly, the unit vector of the landslide downslope direction can be defined as  $s = \begin{bmatrix} \cos \alpha_{slp} \sin \beta_{asp} & \cos \alpha_{slp} \cos \beta_{asp} & -\sin \alpha_{slp} \end{bmatrix}$ , where  $\alpha_{slp}$  is the slope angle and  $\beta_{asp}$  is the aspect of the downslope direction (clockwise from north as positive). Consequently, the downslope movement vector  $M_{dsip}$  can be converted from the radar LOS measurement  $M_{los}$  as  $M_{dsip} = M_{los} / (l \cdot s^T)$ , where  $s^T$  denotes the transpose of  $s$ . The landslide velocities were calculated from the InSAR-measured displacement time series using central difference approximation.

### 3.3. Forced Water Circulation on an Irregular Sliding Surface

#### 3.3.1. Field Evidence and Theoretical Framework

Field and laboratory evidence shows that many slow-moving landslides deform with dominant displacements (commonly >70%) concentrated on the millimeters to centimeters thick basal shear zones (e.g., Collin, 1846; Gould, 1960; Hutchinson, 1970; Keefer & Johnson, 1983; Morgenstern & Tchalenko, 1967; Skempton & Petley, 1968; Ter-Stepanian, 1965; Zaruba & Mencl, 1982), indicating that the landslide mass moves as an approximately rigid block with only minor internal deformation. Slip surface irregularities, such as bumps, steps, depressions, grooves, and striations, are often present and were observed for landslides in California, Utah, France, Norway, Japan, and Italy (Collin, 1846; Guerriero et al., 2014; Mizuno, 1989; Stout, 1971). The asperities are small in general, and the average ratio of height to length is reported as 0.065 by Mizuno (1989). The dynamic behavior of slow-moving landslides commonly comprises very short periods of acceleration and deceleration, leading to relatively steady movements, yet sustained acceleration resulting in rapid motion rarely occurs (Baum & Johnson, 1993; Keefer & Johnson, 1983).

The time-dependent, steady movements can be explained by the forced pore-fluid circulation on irregular basal surface (Baum & Johnson, 1993), which reduces basal pore pressures and regulates downslope landslide motion (Figure 3). Physically, it can be interpreted as that water is forced out of compressed soil on the upstream side of bumps ( $\theta > 0$ , where  $\theta$  is defined and illustrated in Figure 3), whereas water flows through suction toward the downstream sides of bumps ( $\theta < 0$ ). The forced water circulation model simplifies slow-moving landslides as a porous elastic solid sliding over a wavy, impermeable, rigid surface with an average velocity  $\bar{v}_x$  along the  $x$  direction (Figure 3), and the stress and pore water movement in the landslide materials are governed by four equations (Baum & Johnson, 1993; Rice & Cleary, 1976):

$$\frac{\partial T_{xx}}{\partial x} + \frac{\partial T_{zx}}{\partial z} + \rho_s \sin \alpha = 0 \quad (1)$$

$$\frac{\partial T_{zx}}{\partial x} + \frac{\partial T_{zz}}{\partial z} + \rho_s \cos \alpha = 0 \quad (2)$$

$$\nabla^2 \left( T_{xx} + T_{zz} + \frac{1-2\mu}{1-\mu} P \right) = 0 \quad (3)$$

$$\frac{2KG(1-\mu)}{\rho_w(1-2\mu)} \nabla^2 (T_{xx} + T_{zz} + 2P) = \frac{\partial}{\partial t} (T_{xx} + T_{zz} + 2P) \quad (4)$$

where  $T_{xx}$ ,  $T_{zz}$ , and  $T_{zx}$  are the stresses as shown in Figure 3.  $\rho_s$  is the unit weight of the saturated soils,  $\alpha$  is the slope angle,  $\mu$  is the Poisson's ratio for drained deformation,  $P$  is the pore-water pressure,  $K$  is the hydraulic conductivity,  $G$  is the shear modulus, and  $\rho_w$  is the unit weight of water. Equations 1 and 2 are the stress equilibrium equations, Equation 3 is the compatibility equation, and Equation 4 is the stress diffusion equation.

Solving Equations 1–4 requires three boundary conditions based on physical assumptions embedded in the model, defined as

$$[\bar{v}_z]_{z_0} = \bar{v}_x \left( \frac{dz_0}{dx} \right) \quad (5)$$

$$[\tilde{T}_{z\xi}]_{z_0} = 0 \quad (6)$$

$$\left[ \frac{\partial^2 \tilde{P}}{\partial \xi^2} \right]_{z_0} = - \left( \frac{\bar{v}_x \rho_w}{K} \right) \left[ \frac{\partial \tilde{e}}{\partial \xi} \right]_{z_0} \quad (7)$$

where  $z = z_0(x)$  and  $z = z_1(x)$  are the ground surface and the basal slip surface, respectively (Figure 3).  $[\bar{v}_z]_{z_0}$  is the first-order derivative of the landslide motion rate on the slip surface along the  $z$  direction.  $\xi = x - \bar{v}_x t$  is introduced as a new coordinate system, which moves parallel with  $x$  in order to simplify the problem to be independent of time (Rosenthal, 1946).  $[\tilde{T}_{z\xi}]_{z_0}$  is the first-order shear stress on the slip surface,  $\tilde{P}$  is the first-order pore-water pressure, and  $\tilde{e}$  is the volumetric strain. Equation 5 states that the landslide is sliding tangential to the slip surface  $z_0(x)$ . Equation 6 sources from the assumption that the first-order shear stress is zero everywhere on the basal slip

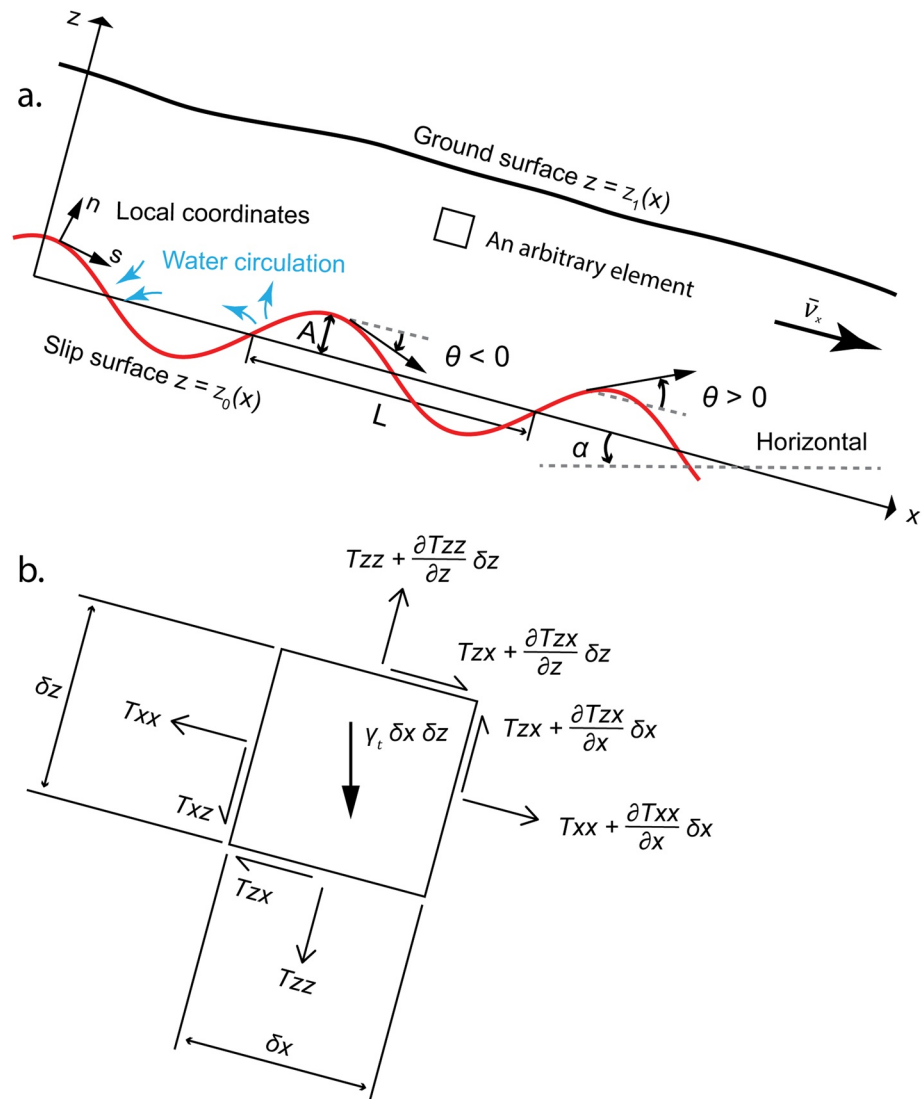


**Figure 3.** Sketch of a landslide block sliding on an undulating, irregular surface. (a) The  $x$  axis is along the average slope of the slip surface, and the  $z$  axis is perpendicular to  $x$ .  $A$  and  $L$  are the amplitude and wavelength of the sine-wave slip surfaces, respectively.  $\alpha$  is the slope angle measured from the  $x$  axis to the horizontal.  $\theta$  is the angle measured counterclockwise from the  $x$  axis to a line tangent to the slip surface at any point. Local coordinates  $n$  and  $s$  are normal and tangential to the slip surface. The blue arrows indicate that that water is flowing away from the upstream sides of the bumps and is flowing toward the downstream sides of the bumps. (b) Stresses acting on an arbitrary element shown in (a). All the arrows point to the positive orientations of the stresses. The figure was modified from Baum & Johnson, 1993.

boundary. Note that this assumption does not consider shear dilation and contraction on the slip surface. Equation 7 relates fluid flow to volume change at the slip surface by using the continuity equation.

Using the above three boundary conditions to solve Equations 1–4 and drop several nonsignificant high-order terms, the average resistance  $R$  that results from the slip surface roughness and acts parallel to  $x$  can be obtained (Baum & Johnson, 1993):

$$R = -\bar{v}_x (Al)^2 \rho_w \frac{(1 - 2\mu)^2}{4KI(1 - \mu)^2} \quad (8)$$

where  $l = 2\pi/L$  is the wave number,  $L$  is the wavelength of sinusoidal asperities on the slip surface.  $Al$ , the product of the amplitude and the wave number, is the maximum local slope of the slip surface with respect to  $x$ . Equation 8 shows that the sliding resistance  $R$  resulting from forced water circulation increases linearly with the

average landslide motion rate  $\bar{v}_x$ . It would consequently contribute to regulating slow-moving landslides from infinite acceleration after the shearing initiates.

### 3.3.2. Simulation of Dynamic Landslide Movement

Following Newton's second law of motion, the force imbalance of the landslide body leads to a positive or negative acceleration  $a_t$  along the downslope direction at time  $t$ :

$$\bar{z}\rho_s g \cdot \sin\alpha - [(\bar{z}\rho_s - h_w\rho_w)\cos\alpha \tan\phi - R] = \bar{z}\rho_s \cdot a_t \quad (9)$$

where  $\bar{z}$  is the average thickness of the landslide material (Figure 3),  $\phi$  is the angle of internal friction,  $h_w$  is the hydraulic head on the slip surface, and  $R$  is the average resistance acting along the downslope direction as shown in Equation 8. Note that Equation 9 is expressed in a general vertical-horizontal Cartesian coordinate system rather than a slope-normal one. The first term on the left in Equation 9 denotes the downslope driving force, and the second term on the left denotes the resistance resulting from normal stress, hydrostatic water pressure, and the resistance from forced circulation on an irregular basal surface. Soil cohesion is not considered in Equation 9 because long-term slow-moving landslides commonly have formed mature slip surfaces that are in a residual state where the bonds of cohesion have broken following rupture. Combining Equations 8 and 9 yields:

$$\bar{a}_t = [g \sin\alpha - g \cos\alpha \tan\phi] + \left[ \frac{\rho_w g h_w \cos\alpha \tan\phi}{\bar{z}\rho_s} - \frac{\bar{v}_t (Al)^2 \rho_w}{\bar{z}\rho_s} \frac{(1 - 2\mu)^2}{4Kl(1 - \mu)^2} \right] \quad (10)$$

where  $\bar{a}_t$  and  $\bar{v}_t = \sum_0^t \bar{a}_t$  are the average acceleration and velocity of the landslide body along the downslope direction at time  $t$ , respectively. We set  $\bar{v}_t \geq 0$  to meet the physical constraint that landslides do not move upslope. The first term on the right side of Equation 10 is a constant if assuming that slope angle and soil mechanical properties do not change during the movement. Hence, the landslide acceleration is essentially controlled by the dynamic, simultaneous evolution of water level rise and the induced resistance increase.

## 4. Results

### 4.1. Mapping Slow-Moving and Catastrophic Landslides

Using SAR interferograms from both the ascending Sentinel-1 track A166 and the descending track D42 between August 2015 and September 2020 as well as satellite optical images from the Google Earth between 1996 and 2020, we identified 13 concurrently active, large, slow-moving landslide complexes and 12 catastrophic landslides in the study region near Hanford, Washington. Geographical locations of the slow-moving landslides S1-S13 and the catastrophic landslides C1-C12 are shown in Figure 2, and their spatial sizes are shown in Table 1. These identified landslides dominantly occurred at the bluffs along the eastern bank of the Columbia River. The destabilized bluffs (31.3 km) occupy 50.2% of the eastern riverbank in the study region (62.1 km).

The largest active landslide complex in the region is the Wiehl Ranch landslide complex (S2), which consists of multiple landslides and stretches by  $\sim 7.5$  km along the Columbia River bank (Figure 2). Each individual landslide within the complex measures  $\sim 750$  m in the longitudinal direction and 200–750 m in the transverse direction. The Wiehl Ranch landslide complex has also been expanding south rapidly from 1996 to 2020, potentially resulting from water infiltration from the wastewater pond 4 km east of the landslide headscarp (Figure 2b). The largest catastrophic runout landslide (C1) in the region occurred near the Savage landslide complex in June 2017, which inundated a 940 m by 830 m (length by width) area along the hillslope. Following the 2017 runout failure, the destabilized landslide materials evolved into a slow-moving landslide and remained active by September 2020 based on InSAR observations (Figures 2 and 4). This is a typical example of landslide sites that have hosted both slow-moving and catastrophic slides in the past (Figure 2). In addition, the 2020 true color image (Figure 2b) shows that all of the identified active landslides are located on the eastern side of the Columbia River, where the vast area of irrigated farmlands (in green hues) exists.

Annual surface movement rates at different locations within an individual landslide complex vary significantly, which indicate that the landslide complexes are composed of multiple, relatively independent slides moving toward the Columbia River. For example, the northernmost section of the Locke landslide complex (S1) had a



**Table 1**  
*Spatial Size and Disturbing Forces of the Identified Active Landslides*

Slow-moving landslide complexes				Catastrophic landslides	
Name	Length by width (m)	Riverside slide?	Dominant force disturbances after landslide initiation	Name	Length by width (m)
S1	900 × 6,200	✓	Columbia River water level	C1	890 × 810
S2	870 × 7,500	✓	Columbia River water level	C2	360 × 250
S3	320 × 3,400	✓	Columbia River water level	C3	1,100 × 300
S4	880 × 3,300	×	Irrigation water infiltration Basal geometry	C4	480 × 270
S5	800 × 2000	×	Irrigation water infiltration Basal geometry	C5	200 × 270
S6	280 × 320	×	Irrigation water infiltration	C6	700 × 370
S7	340 × 340	×	Basal geometry	C7	280 × 70
S8	910 × 1,900	×	Irrigation water infiltration	C8	340 × 210
S9	240 × 280	×	Irrigation water infiltration	C9	320 × 90
S10	230 × 1,300	×	Irrigation water infiltration	C10	340 × 180
S11	230 × 740	×	Irrigation water infiltration	C11	410 × 240
S12	720 × 1,200	✓	Columbia River water level	C12	850 × 580
S13	610 × 2,000	×	Irrigation water infiltration		

3.3 cm/year Line-of-Sight (LOS) motion rate between 2015 and 2020 from the ascending Sentinel-1 SAR images, whereas the central section moved at only 1.5 cm/year and some sections remained almost static (Figure 4a). Similarly, the Savage landslide complex (S5) experienced the fastest deformation (2–3 cm/year along A166 LOS direction) at the northernmost and the southernmost sections, whereas the central section moved at only 0.4 cm/year (Figure 4a). The individual landslides within a complex are also distinguishable based on their headscarp morphology (Figure 4). Additionally, the identified large catastrophic landslides (e.g., C1, C6, and C12) were commonly initiated at their steep headscarps proximal to irrigated farmlands (Figure 4b) and were activated during periods of intensive irrigation (April to October), which indicate that irrigation water was likely responsible for triggering. The inundation extents vary depending on the source volume and basal geometry (Figure 4b).

## 4.2. Kinematics of Slow-Moving Landslides

### 4.2.1. The Slow Life Cycle From Initiation to Deposition

In order to characterize the life cycle of slow-moving landslides triggered by agricultural irrigation near Hanford, Washington, we measured and integrated the motion dynamics of the Locke landslide (S1) and the southernmost section of the Savage landslide (S2) to demonstrate the typical behaviors. During our satellite observation period from 1996 to 2020, the Locke landslide had already evolved toward later stages of activity (i.e., motion cessation and final deposition; Figure 5), whereas the southern Savage landslide was freshly initiated and subsequently evolved toward gradual deceleration (Figure 6). Both landslide complexes were initiated in a similar manner by water infiltration from nearby wastewater ponds and progressed similarly by advancing forward toward the relatively flat Columbia River bed, where they began to slow down.

Figure 5 illustrates the 2020 landscape of the Locke landslide complex. This landslide complex was initiated by irrigation water, which was diverted to a wastewater pond ~1 km east of the landslide (see Figure 2) in the late 1960s for the purpose of enhancing wildlife habitat. The landslide block slumps began in the 1970s and peaked around 1985 (Bjornstad & Peterson, 2019). The wastewater pond was completely drained in the mid-1990s in an effort to mitigate landsliding; however, landslide creep continues to the present day at a maximum rate of 9.3 cm/year along the downslope direction (Figure 4a). From 1965 to 2020, the advancing landslide toe has shifted the Columbia River bank westward by up to 260 m (Figure 5), which also exacerbated riverine erosion of the Locke Island by approximately 42 m since 1994 (Bjornstad, 2006). Aeolian sands cover the large unirrigated lands east of the landslide (Figure 5a; Figure 2b), whereas water seepage and sag ponds (about 37 m above the Columbia River surface in elevation) are clearly present near the landslide headscarp, which indicate irrigation water infiltration as the primary landslide trigger.

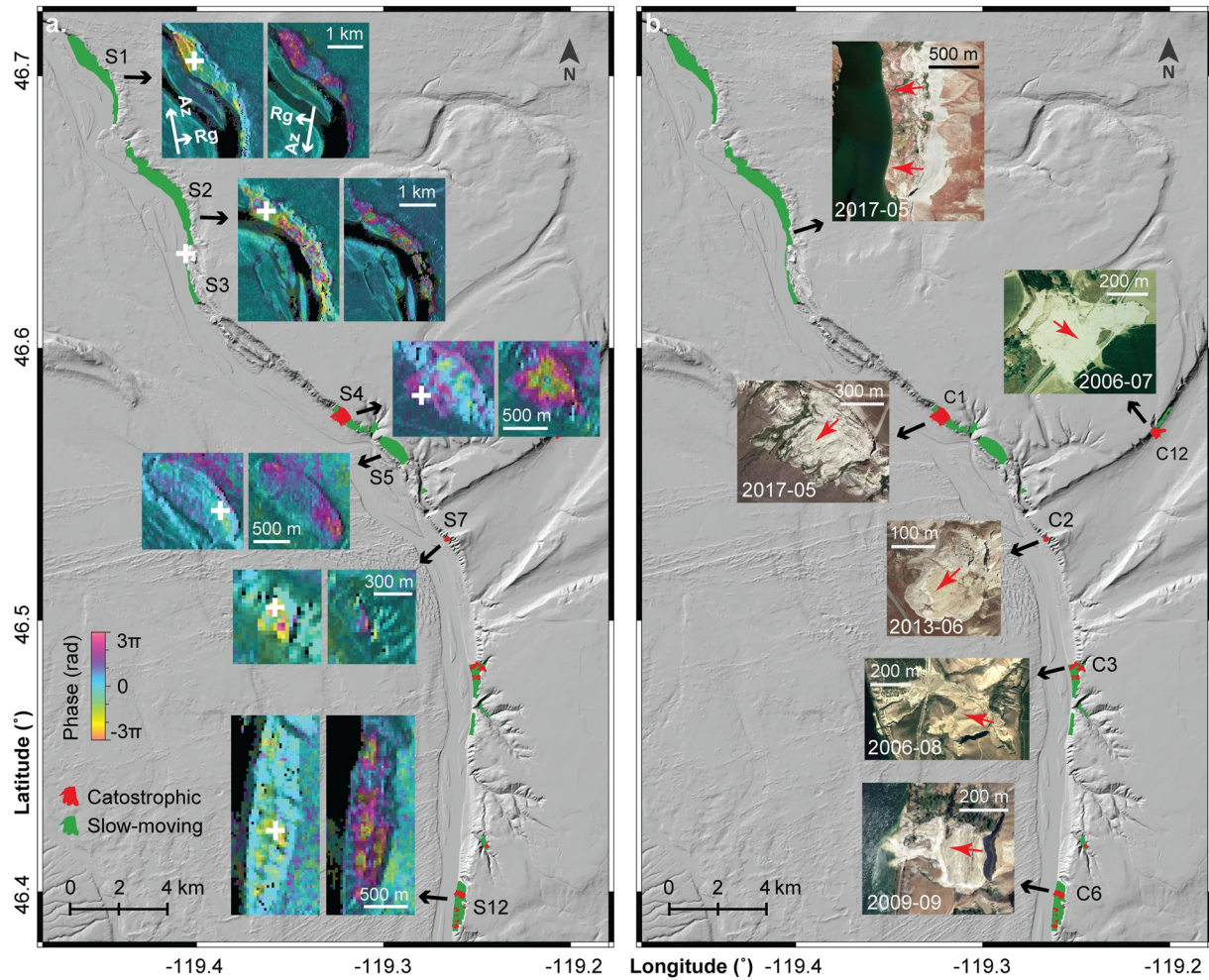


**Figure 4.** Landslides observed from space. (a) Stacking synthetic aperture radar (SAR) interferograms from 2016 to 2020 for six typical slow-moving landslide complexes, showing the averaged line-of-sight (LOS) displacement rates. For each slow-moving landslide, the left SAR interferogram was produced from ascending Sentinel-1 images (track 166), and the right one was from descending images (track 42). A full color fringe from red to violet on the SAR interferograms represents a line-of-sight displacement of 33.6 cm. The white “+” symbols mark the selected points for time-series analyses. (b) Google Earth true color images of the southernmost section of the slow-moving landslide complex S2 (the topmost inset) and the six catastrophic landslides C1–C6. The year and month of image acquisition are labeled. Landslide motion directions are marked with red arrows.

Similar to the Locke landslide complex, the southern Savage landslide complex shares analogous geological and topographical settings and was also triggered by elevated groundwater stemming from irrigation. The primary water source was potentially from the wastewater pond 3.1 km east of the landslide headscarp (Figure 2b). Landslide initiation likely occurred in 2003 at the very southern end of the landslide complex (Figure 6). As measured from Google Earth optical images, the motion rates peaked at 22.5 m/year between 2003 and 2006, followed by subsequent gradual rate decreases to 17.3 m/year by 2009, 12.4 m/year by 2011, 10.3 m/year by 2013, and 6.1 m/year by 2020 (Figure 6). Note that the estimations of the shoreline position are more sensitive to river level fluctuations after 2015 as the landslide toe began to advance nearly horizontally and more slowly. Following the deceleration trend, it can be projected that the movement of the southern Savage landslide will reduce to 9.3 cm/year (current maximum rate of the Locke island) at 40 years after initiation by using an exponential fitting  $v_r = 22.65 e^{-0.09755 \cdot t_r}$  ( $R^2 = 0.998$ ), where  $v_r$  is the motion rate and  $t_r$  the time. The estimation is comparable to the 35 years for the Locke landslide complex during which the landslide motion dropped from peak rate to the current state.

By integrating motion dynamics of both the Locke landslide and the southern Savage landslide, it can be concluded that the irrigation-triggered slow riverside failures near Hanford move with an exponentially decreasing rate after instigation and rapid acceleration to the peak rate.



**Figure 5.** Landscape of the Locke landslide complex (landslide S1). (a) Active sand dune near headscarps of the Locke landslide, which corresponds to the bottom-left-corner region in (b). Note the human in the photo for scale. (b) A photo of the Locke landslide adapted from Bjornstad & Peterson, 2019.

#### 4.2.2. Slow Motion Modulated by External Controls

Over a long timescale (e.g., tens of years), slow-moving landslides can be characterized by a short-period acceleration followed by a subsequent period of slow motion that is an order of magnitude longer (Figure 6). However, within short timescales (e.g., weeks to months), external controls such as groundwater variation from irrigation water and the Columbia River strongly modulate landslide motion. Note that surface precipitation mostly evaporates and does not contribute to groundwater in the desert climate near Hanford: the annual evaporation rate of 213 mm/year (Martens et al., 2017) exceeds the annual precipitation of 180 mm/year (Figure 8d).

Figure 7 shows the time-series LOS displacements of seven slow-moving landslides from ascending and descending Sentinel-1 InSAR measurements between 2015 and 2020. The ascending and descending InSAR measurements of the slow-moving landslides S1, S2, S3, and S12 correspond to exactly the same  $3 \times 3$  pixel array ( $30 \times 30$  m), whereas the measurements for landslides S3, S4, and S5 correspond to slightly different neighboring pixels (within 100 m) because of coherence loss in one or more of the selected SAR interferograms at the ideal corresponding pixel location. For the landslide S4, a runout event occurred in June 2017, which caused severe coherence loss and consequently broke the InSAR time-series measurements into two halves. We manually bridged the pre-event and post-event displacement times series together using the average motion rates immediately before and after the June 2017 runout event.

As can be seen from Figure 7, the annual motion rates of different slow-moving landslides vary considerably. Landslide S2 moved the fastest with a mean ascending LOS rate of 8 cm/year and a descending LOS rate of 14 cm/year, whereas the landslide S5 moved the slowest with a mean ascending LOS rate of 1.2 cm/year and a descending LOS rate of 3.6 cm/year. However, landslides with similar geomorphic settings share anomalous



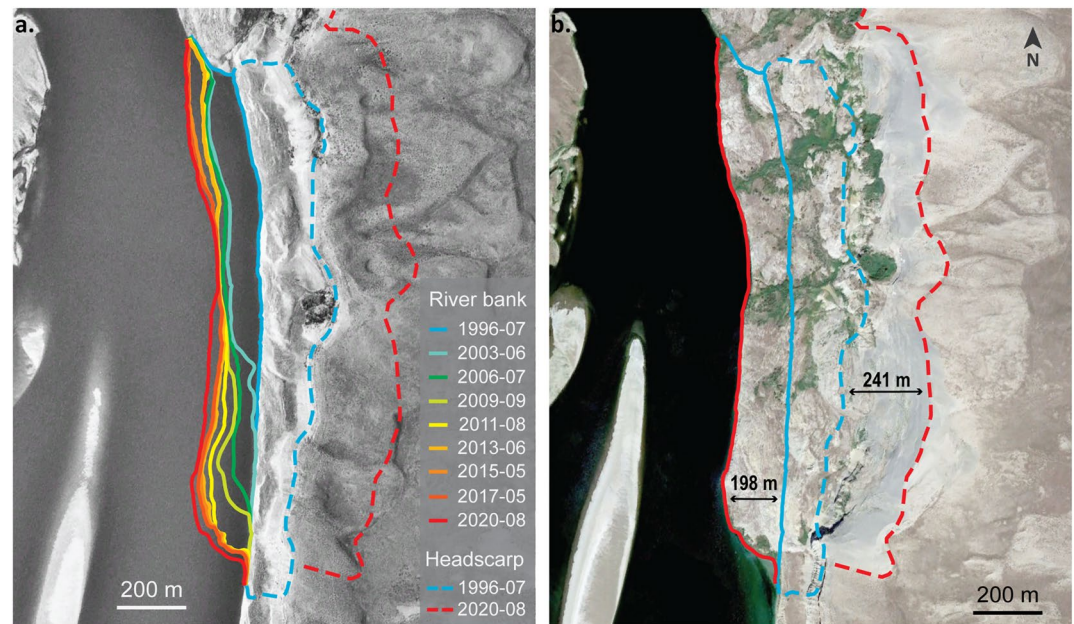


**Figure 6.** Landslide evolution at the southern end of the Wiehl Ranch landslide complex (landslide S2). (a) Advancing front of the landslide toe above the Columbia River from 1996 to 2020. The year and month of the image acquisition are labeled in the legend. The background image was acquired in July 1996 and accessed from Google Earth. (b) Advance of landslide toe and retrogression of landslide headscarp. The background image was acquired in August 2020 and accessed from Google Earth.

movement fluctuations. For example, the four riverside landslides (i.e., S1, S2, S3, and S12) with landslide toes in the Columbia River manifested simultaneous acceleration in February 2017, April 2018, April 2019, and April 2020 though their absolute motion rates vary (Figure 7). A detailed comparison of their motion rates with water level of the Columbia River demonstrates that the observed four major accelerations were primarily associated with water level rise of the river (Figure 8) and potentially related riverbank erosion. Accelerations occurred when the river water level reaches a threshold of approximately 5 m.

In contrast, landslides distant from the Columbia River (i.e., S4, S5, and S7) exhibited motion dynamics unrelated to the river water levels (Table 1). The short-term accelerations of the river-distant landslides S4, S5, and S7 mostly likely resulted from irrigation water seepage as these landslides are all located at the margin of the irrigated farmlands and the major accelerations occurred during the irrigation season (April to October). Note that exact irrigation schedules might vary spatially and temporally depending on the crop types. The long-term motion trend of the river-distant landslides (S4, S5, S7) exhibited linkages to the surface topography. For instance, the landslides S4 and S7 with long and nearly planar basal slopes maintain nearly constant motion rates after 2018, whereas the landslide S5 with a concave-up basal slope gradually slowed down as advancing downslope from 2015 to 2020.

Unlike many slow-moving landslides near the U.S. West Coast, which are strongly regulated by seasonal precipitation (e.g., Handwerger et al., 2013; Xu et al., 2019; Xu et al., 2020), ground precipitation in the desert near Hanford, where evaporation exceeds precipitation, does not show obvious contribution to the landslide motions (Figure 8d). For example, the water years 2017–2018 and 2018–2019 experienced less cumulative precipitation but much greater displacement than water years 2016–2017 and 2019–2020 (Figure 8), which is in contrary to the typically rainfall-driven landslide behaviors in the U.S. West Coast where annual precipitation is abundant (e.g., Handwerger et al., 2013; Xu et al., 2019; Xu et al., 2020).



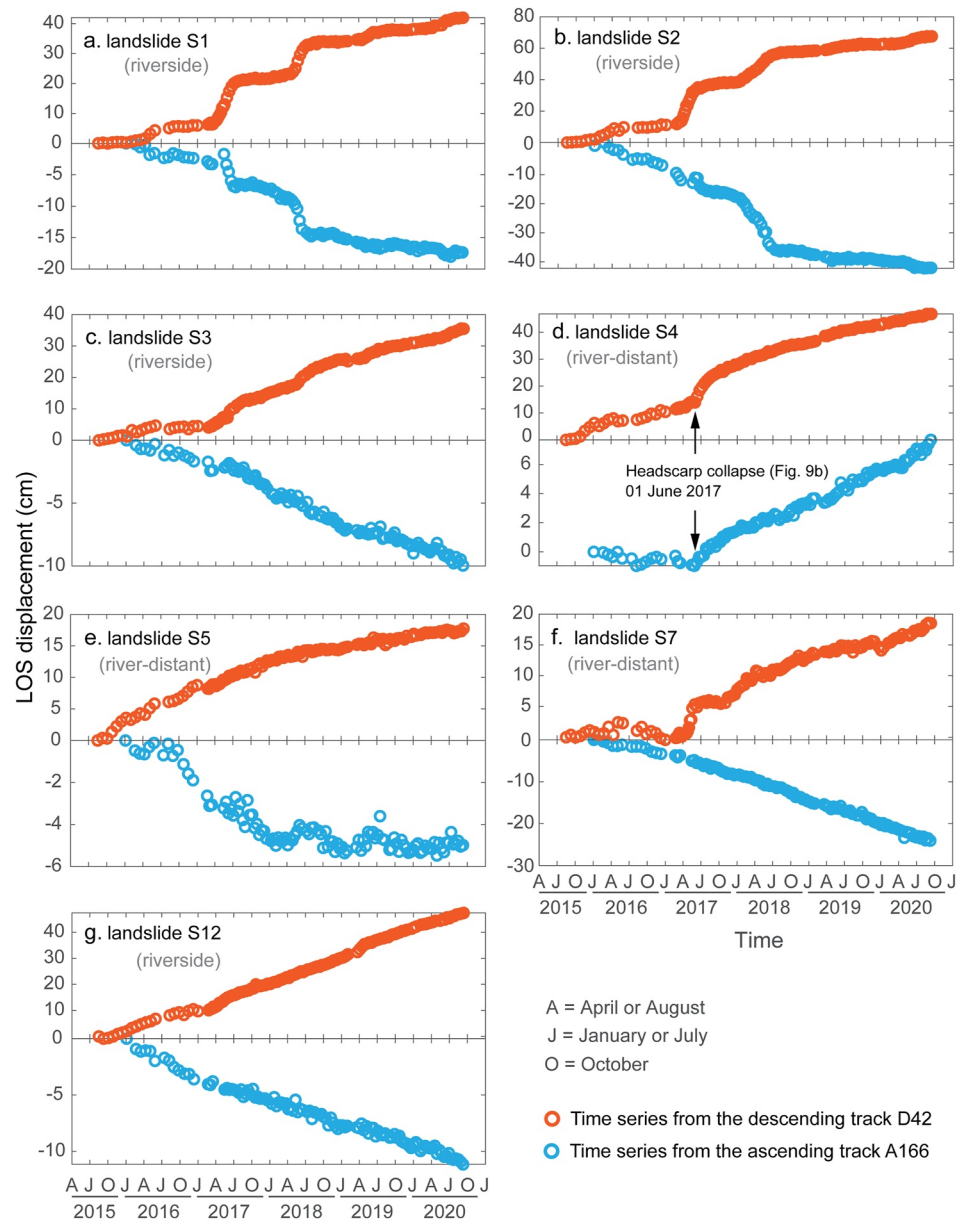


**Figure 7.** Time-series displacements of seven slow-moving landslides between July 2015 and October 2020 from Sentinel-1 interferometric synthetic aperture radar (SAR) measurements. Geographical locations of the selected measurement points for the landslides are depicted in Figure 4. (a, b, c, and g) show displacement measurements of a same geographical point from ascending (A166) and descending (D42) SAR data for each individual landslide. (d, e, and f) show measurements at slightly different locations (within 100 m) on a landslide from ascending and descending data because of coherence loss in one of the SAR data sets. Positive line-of-sight displacements denote distance shortening between ground targets and the satellite.

#### 4.3. Kinematics of Catastrophic Landslides

Different from the prolonged life cycle of slow-moving landslides (e.g., tens of years), catastrophic runout landslides usually undergo a full life cycle from initiation to deposition within several days, with dominant movements completing within minutes to hours (Bjornstad & Peterson, 2019). Figure 9 shows photos of three catastrophic landslides (C12, C1, and C6) that occurred between 2006 and 2017 in the study region. The catastrophic landslide C12 failed on 20 August 2008 at Basin Hill (Figure 2). It traveled downslope by about 850 m after an abrupt failure at the headscarp and inundated a region with a planform area of  $2.4 \times 10^5 \text{ m}^2$ . The debris buried a 390-m-long segment of a county road (Road 170) and almost destroyed a local farm worker's home (Figure 9a).

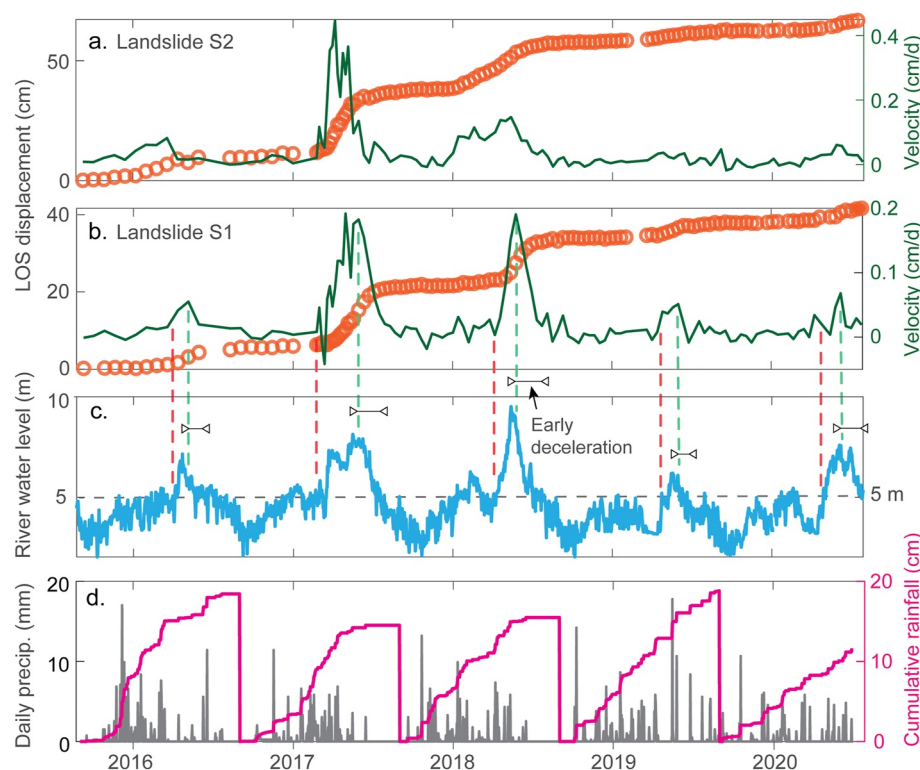


**Figure 8.** Relationship of landslide movement with regard to rainfall and groundwater level for the riverside slow-moving landslides S1 and S2. (a) Orange circles denote line-of-sight (LOS) displacements of the landslide S2 from the Sentinel-1 descending track D42. The green polyline shows the corresponding movement velocity as scaled by the green labeling on the right. (b) Movement measurements of the landslide S1 with same labeling rules as (a) and (c) water level of the Columbia River from a river gauge below the Priest Rapids Dam. The horizontal bars denote the time lengths of the observed early deceleration from peak velocity to river height dropping below 5 m. (d) Gray bars depict daily precipitation at the Saddle Mountain meteorological station (18 km west of the landslide complex S1). The pink polyline shows cumulative rainfall starting from September 1 of each year and follows the vertical labeling on the right. The red vertical lines between (b) and (c) mark the time when the landslide S1 started to accelerate each year, and the green vertical lines mark the time when the landslide began to decelerate.

Landslide C1 occurred in early June 2017 and evolved into a typical “hourglass”-shaped earth flow, which traveled downslope by  $\sim 890$  m. Accelerated deformations were captured starting approximately 36 days before the runout failure by three Sentinel-1 acquisitions, and the formed flow deposits remain actively moving as of September 2020 (Figure 7d). Before the largest June 2017 runout event, multiple small debris flows occurred from a retrogressive failure at the same headscarp since 2003 as captured by Google Earth optical images. These headscarp failures were directly triggered by excessive water from the sprinkler irrigation at and near the landslide headscarp, which were also evidenced by large amounts of water seeping out of the bluff (Figure 9b and Bjornstad & Peterson, 2019). Similarly, landslide C6 was triggered by water seepage from irrigated farmlands near the Johnson landslide complex (Figure 9c). It failed abruptly on 13 May 2006 and evolved into a mobile debris flow, which transported large amounts of sediment downslope into the Columbia River. The sediment traveled further south with the average water flow of 3.08 m/s in the Columbia River (USGS, 2021c) and formed clearly observable silt plumes as far as 7.2 km downstream of the landslide toe (Figure 9d).

To summarize, the catastrophic landslides C12, C1, and C6 vary in geographical locations but were all similarly triggered by irrigation water seepage at their steep headscarps. They all failed abruptly and evolved into relatively mobile debris flows, which inundated areas over 10 times larger than the landslide source. Compared to the prolonged life cycle of slow-moving landslides, these catastrophic landslides completed the process from initiation to deposition within 1 day (Bjornstad & Peterson, 2019). The majority of the deformation might complete within minutes to hours depending on the landslide mobility, but no temporally dense observations are available for verification.

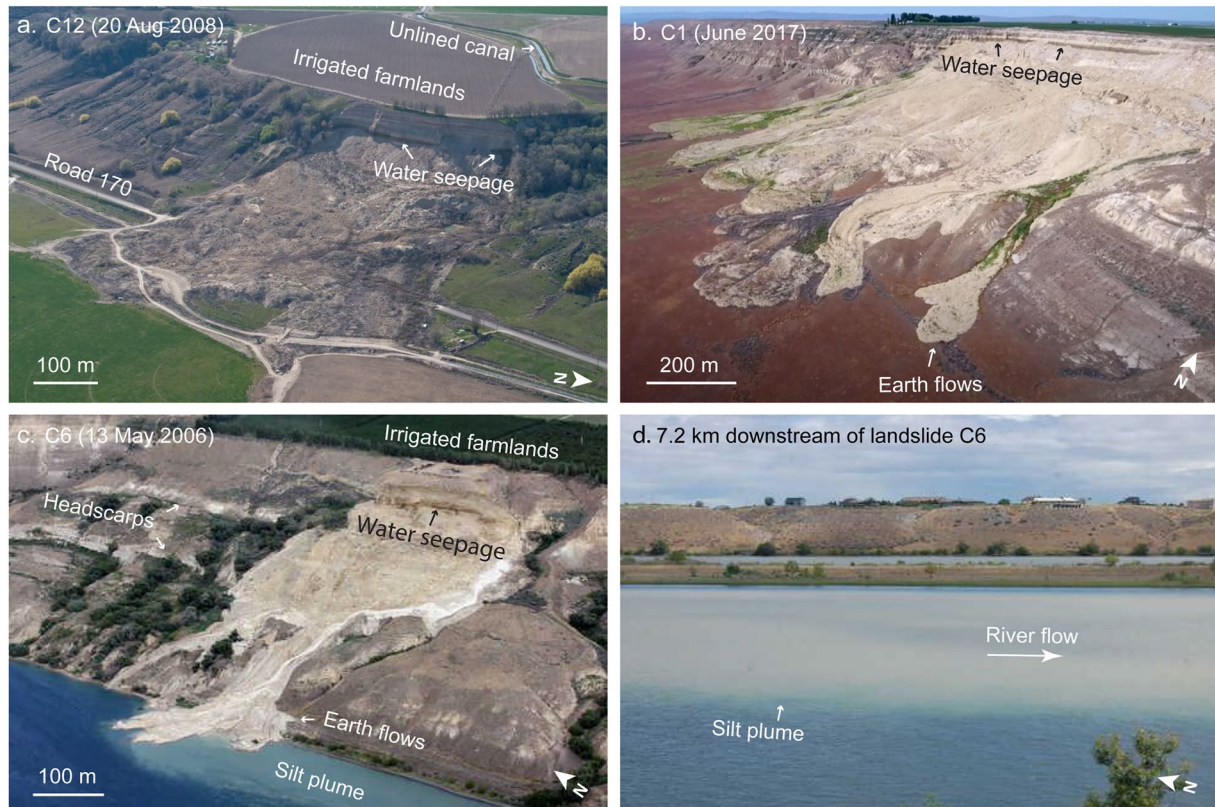


**Figure 9.** Post-failure photos of catastrophic landslides at Basin Hill (C12), the Savage landslide complex (C1), and the Johnson landslide complex (C6). (a–c) depict the post-failure debris flows of the three catastrophic landslides, respectively. (d) Shows the silt plume produced by the landslide C6. Photos in (a, c, and d) were adapted from Bjornstad & Peterson, 2019.

#### 4.4. Basal Surface Roughness Regulates Slow-Moving Landslides by Forced Water Circulation

Owing to the unique hydrogeological histories and settings of the slow-moving Locke landslide complex, here we take it as a typical example to investigate the potential regulation of slow-moving landslide motions by forced water circulation on an irregular basal surface. Note that the resisting force generated from forced water circulation is generally too small to halt a catastrophic landslide (Baum & Johnson, 1993).

##### 4.4.1. Hydrogeological Settings of the Locke Landslide

As introduced in Section 4.2.1, the Locke landslide complex was initiated by water infiltration from a wastewater pond, which was later completely drained in mid-1990s (Bjornstad & Peterson, 2019). In the desert climate near Hanford (Peel et al., 2007), surface precipitation also contributes little to groundwater. Hence, the groundwater level within the Locke landslide complex was dominantly controlled by water level of the Columbia River where 44% of the landslide body resides (approximately 250 m long). This was also verified by piezometer measurements from 10 boreholes drilled on and near the landslide complex in 1998 and 1999 (Bennett et al., 2002). Four boreholes were drilled in 1998 along a north-south-oriented line approximately 500 m east of the landslide headscarps, four were drilled much farther east of the landslide complex (over 1 km) in 1998, and two others were drilled on the landslide toe (Figure 10). The borehole piezometer measurements suggest that the far east side of the landslide was completely dry from 1988 to 2002, whereas the groundwater levels within 500 m east of the landslide complex were almost the same as the Columbia River surface at 114.6 m above sea level. Additionally, borehole measurements revealed that landslide thicknesses were 16.6 m at the borehole BH-1 (17.1 m deep) and 14.8 m at the borehole BH-2 (20.1 m deep) (Figure 10; Bennett et al., 2002). The slip surface materials are composed of homogeneous, fine-grained, medium-to high-plasticity clay, which overlay Quaternary river alluvium (a heterogeneous mixture of cobbles and gravels deposited by the Columbia River) or differentially cemented sands (Bennett et al., 2002).



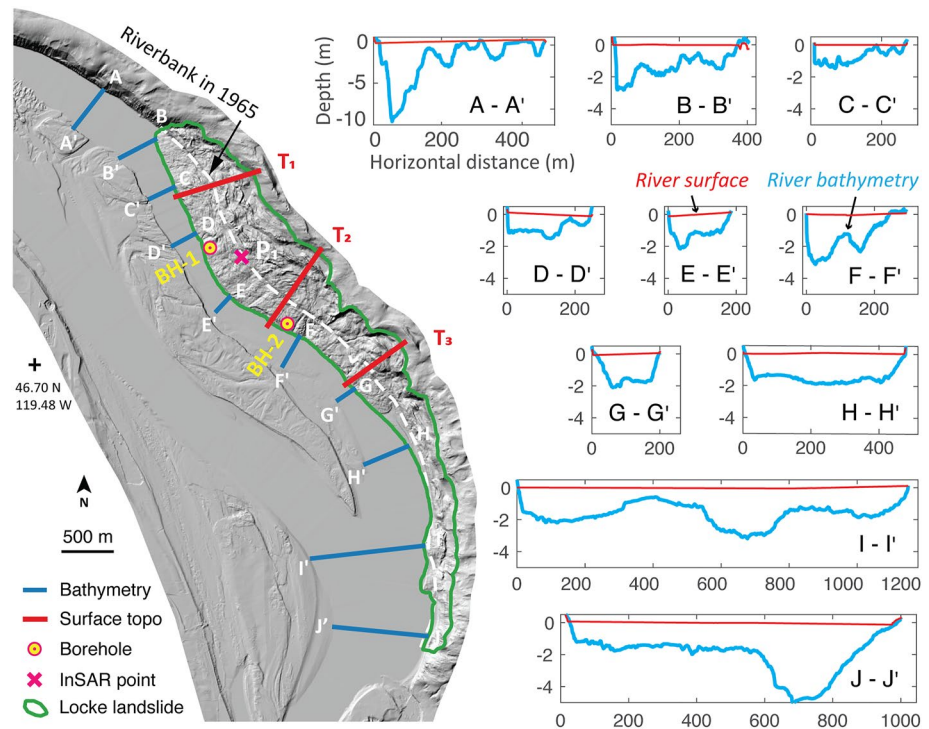


**Figure 10.** River bathymetry near the Locke landslide complex. The hillshade map on the left was produced from the 2010 Columbia River bathymetry data, which were obtained from the Washington Department of Natural Resources. Geographical locations of the Interferometric synthetic aperture radar measurement point  $P_1$ , 2 boreholes, 3 surface topography transects, and 10 river bathymetry transects were illustrated on the hillshade map. River bathymetry data of the 10 selected transects, A-A' to J-J', are shown in 10 corresponding panels on the right, in which river bathymetry is depicted in light blue polylines and river surface in red polylines.

As depicted in Figure 10 and suggested by the borehole logs (Bennett et al., 2002), about half of the landslide body near the InSAR measurement point is lying over and sliding on the previous Columbia River bed. Hence, we can infer the slip surface geometry of the landslide by using bathymetry data of the current Columbia River near the landslide complex. By illustrating 10 cross sections of the river, our results show that the Columbia River bed is highly irregular. If using sine waves to fit the undulating riverbed, the amplitudes of the sine waves vary from 0.5 to 10 m, and the wavelengths range from 45 to 620 m. In general, the bathymetry transects that were not affected by the advancing landslide body (i.e., I-I', J-J', and A-A') show much greater wavelength and amplitude for the undulations, whereas the river transects that were narrowed down by the advancing landslide present smaller asperities in both wavelength and amplitude. Considering that the river bed near the InSAR measurement point  $P_1$  was more likely to be similar to the transects A-A' and B-B' before the landslide body advanced into the river, we incorporated these 10 bathymetry transects to provide an estimate of the wavelength and amplitude of the slip surface near the point  $P_1$  as 10 and 0.6 m, respectively (Table 2).

#### 4.4.2. Numerical Simulations of the Early Deceleration by Forced Water Circulation

Figure 8 shows that the Locke landslide (at the InSAR measurement point  $P_1$  in Figure 10) began to accelerate when the water level rose to approximately 5 m every year, from 2015 to 2020, which can be attributed to the elevated basal pore pressure within the landslide body. However, when the Columbia River height slightly passed the peak yet remained above 5 m (i.e., 5.8 m in 2016, 6.4 m in 2017, 8.2 m in 2018, 5.3 m in 2019, and 6.9 m in 2020), the landslide started to decelerate, which is in contradiction to the simple infinite slope assumption that landslides keep accelerating when the driving force exceeds shear resistance. Here, we attempt to explain the observed “early deceleration” phenomenon using the forced water circulation as introduced in Section 3.3.



**Table 2**

*Model Parameters for Simulating the Resistance From Forced Water Circulation at the Locke Landslide Complex*

Parameters	Value	Reference
Gravitational acceleration, $g$	9.8 m/s <sup>2</sup>	—
Density of water, $\rho_w$	$1 \times 10^3$ kg/m <sup>3</sup>	—
Density of saturated soil, $\rho_s$	$2.1 \times 10^3$ kg/m <sup>3</sup>	Chugh & Schuster, 2003
Average basal slope angle, $\alpha$	18°	Chugh & Schuster, 2003
Internal friction angle, $\phi$	21°	Bareither et al., 2012
Average landslide thickness, $\bar{z}$	15.7 m	Bennett et al., 2002
Poisson's ratio, $\mu$	0.3	Bennett et al., 2002
Hydraulic conductivity, $K$	$5 \times 10^{-8}$ m/s	Baum & Johnson, 1993
Average amplitude of basal asperities, $A$	0.6 m	Figure 10
Average length of basal asperities, $L$	10 m	Figure 10

Every year, seasonal water release from the upstream Priest Rapids Dam elevates the water level of the Columbia River and increases basal pore pressures within the submerged portion of the riverside landslides near Hanford, thereby causing these slow-moving landslides to accelerate. However, the increased movement velocity strengthens the forced water circulation on the irregular landslide basal surface, which tends to stabilize the landslide by enhancing shear resistance, and therefore requires a much higher hydraulic head (water level of the Columbia River) to keep the landslide moving (Figure 8). Because the forced water circulation induced a significant pore pressure reduction, which cannot be fully compensated by the elevated water levels, the landslide decelerates. The landslide stops completely once the water level drops below the 5 m threshold until another period of high water-reactivated landslide motion (Figure 8). In general, the landslide velocity correlates linearly with excess groundwater levels (the part exceeding the threshold groundwater condition), which well matches the predictions of the forced water circulation model (Equation 8).

To quantify the resistance from the forced water circulation and its impact on motion kinematics of the Locke landslide, we employed Equation 10 to simulate the dynamic motion evolution using river gauge data of the Columbia River from 2016 to 2020 (see details in Section 3.1). Geometrical, mechanical, and hydrological parameters of the Locke landslide are summarized in Table 2. The mechanical properties of the landslide materials were compiled from field and lab test results in published literature (Bareither et al., 2012; Bennett et al., 2002; Chugh & Schuster, 2003). Using the constants listed in Table 2 as inputs for Equation 10, the river height  $h_w$  is the only variable to drive dynamic evolution of the landslide velocity.

As shown in Figure 11, our results show that by including the forced water circulation, the simulated landslide dynamics match the InSAR observations very well in terms of both the response time and movement velocity. Here, the landslide velocities were converted from the radar LOS direction to the downslope direction using the method detailed in Section 3.2.2 with  $\theta_{inc} = 39.2^\circ$ ,  $\phi_{head} = -170.3^\circ$ ,  $\alpha_{slp} = 18^\circ$ , and  $\beta_{asp} = 234^\circ$ . From the simulation, the predicted deceleration dates in years 2016 to 2020 approximate the observed dates with differences by 8, 9, 10, 1, and 2 days, respectively. Note that InSAR-derived deceleration dates have an uncertainty of 12 days (before January 2017) or 6 days (after January 2017) due to the satellite revisit cycle. The simulated maximum velocity occurred in 2017 summer at 0.53 cm/day, which is very close to the InSAR-measured 0.47 cm/d. In contrast, if excluding the forced water circulation and simply using the infinite slope assumption, the simulated results differ from the InSAR observations drastically. For example, the predicted deceleration dates would deviate from the observed dates by 26, 46, 68, 14, and 42 days in 2016 to 2020, respectively. Effectively, the decelerations would only occur after the river height dropped below the 5 m threshold. The maximum movement velocity is also substantially overpredicted to 32.6 cm/d in the 2017 summer, which is about 69 times greater than the InSAR observations.

A systematical evaluation of parameter sensitivities of the forced water circulation model was provided in Baum and Johnson (1993). In general, the basal surface roughness  $Al$  can vary by one order of magnitude to match the observed landslide peak velocity and the timing of early deceleration. To summarize, the shearing resistance

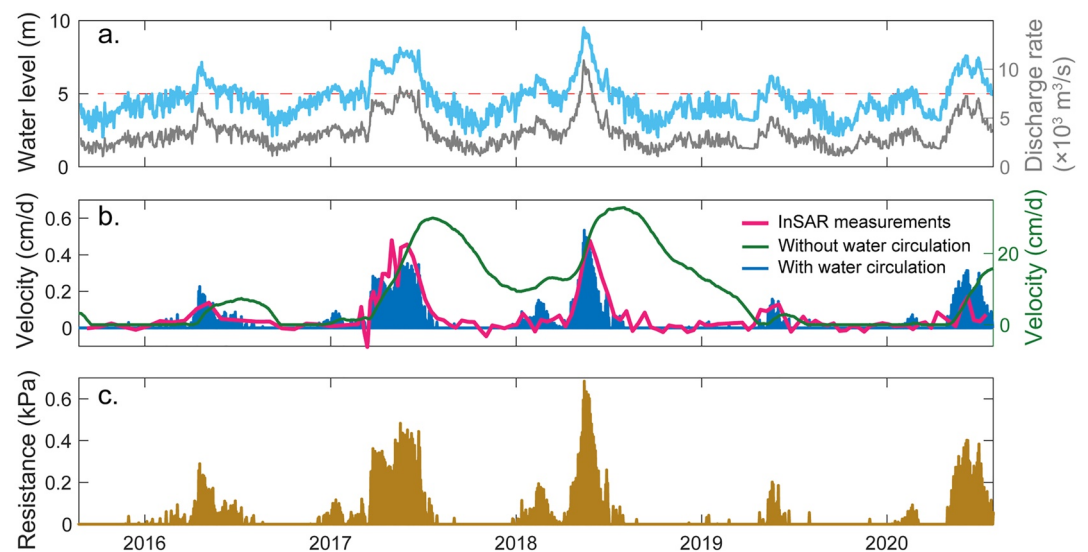


**Figure 11.** Simulated dynamic movement of the Locke landslide near the interferometric synthetic aperture radar (InSAR) measurement point. (a) Water level (blue line) and discharge rate (gray line) of the Columbia River. (b) Downslope movement velocity of the landslide from InSAR observations (red polyline) and numerical simulations (blue bars and green polyline). The red polyline and blue bars follow the y-axis labeling on the left, whereas the green polyline follow the y-axis labeling on the right. Here, the InSAR-captured line-of-sight velocities (shown in Figure 8b) were converted to the downslope direction to allow direct comparison with the model simulations. (c) Calculated resistance from forced water circulation.

generated from forced water circulation on an irregular surface may regulate landslide velocity and motion kinematics significantly. Such impacts could have been the primary cause of the early decelerations observed at the Locke landslide complex.

#### 4.5. Basal Surface Steepness Bifurcates Slow and Catastrophic Movements

Our satellite observations show that slow-moving landslides and catastrophic landslides coexist in some of the landslide complexes near Hanford (Figure 4). However, such contrasting motion behaviors cannot be well explained by the forced water circulation, which is unable to generate sufficient resisting force to halt a fast-moving landslide (Baum & Johnson, 1993). We therefore investigated other potential factors, which might have contributed to their contrasting post-initiation motion behaviors.

As a typical example, the Johnson landslide complex contains six catastrophic landslides (C6–C11) and multiple large, slumping landslide blocks (Figure 12). Except for the landslide C6 which occurred in 2006, all of the other slow-moving landslides and catastrophic landslides were initiated before 1996. The entire Johnson landslide complex was activated by a nearly linear rise of groundwater level after 1971 due to excessive agricultural irrigation (Figure 13). By 1983, the groundwater level had elevated to 3.3 m below the ground surface at the monitoring well 1 km east of the Johnson landslide complex before leveling off.

As can be seen in Figure 12, all of the slow-moving landslides are composed of large, deep-seated and relatively intact slump blocks, whereas the catastrophic landslides typically source from small failures at the steep headscarps. Consequently, the basal geometry (including the slip surface and topography downslope of the landslide mass) might have been a decisive factor that bifurcates the post-initiation kinematics of these contrasting landslides. To further elucidate the potential impacts of basal geometry on landslide post-initiation behaviors, we analyzed the slip surfaces of five slow-moving landslides and five catastrophic landslides over the entire study region by differentiating their topographical characteristics. The topographical profiles were produced or inferred from 2010 lidar DEMs, the National Elevation Datasets, the 2001 Shuttle Radar Topography Mission (SRTM) DEMs, the 1924 topographical maps, and Google Earth optical images. Topographical features, including location and dip angle of landslide headscarp, internal cracks, and landslide toes, were integrated to infer basal surface of the slow-moving landslides.



**Figure 12.** Landscape of the Johnson landslide complex (S12 and C6–C11). The background photo was adapted from Bjornstad & Peterson, 2019.

As shown in Figure 14, we plotted elevation profiles of the selected 10 landslides along their commensurate downslope directions under identical geographical scales. First, a straightforward comparison of basal slope angles of the slow-moving landslides and the catastrophic landslides reveal that the catastrophic landslides are dominantly seated on much steeper basal surfaces than slow-moving landslides. Second, catastrophic landslides have steeper topographical settings immediately below the landslide toe than slow-moving landslides, precluding potential buttressing effects with downslope advance. Third, slow-moving landslides tend to be deep-seated and involve movement of a large amount of soil/rock mass. Mechanically, a steep basal surface and downslope path allow landslide materials to gain more kinetic energy from potential energy drop when moving by the same downslope distance, which are more likely to maintain landslide velocity and are less affected by localized topographic asperities. The magnitude of landslide volume is essentially controlled by pre-landslide surface topography with other contributing factors being equal.

Basal geometry also strongly affects motions of slow-moving landslides. For example, the landslide S5 has been slowing down from 2015 to 2020 (Figure 7e), potentially because the landslide toe touches an adversely sloped hill that would effectively resist the landslide's downslope motion (Figure 14). The landslide S12 (here referring to the landslide slightly north of the landslide C6 in Figure 12) formed steep and large headscarps yet did not fail as abruptly as the neighboring landslide C6, potentially because it has a deep-seated and gently sloped basal surface, especially at the toe section.

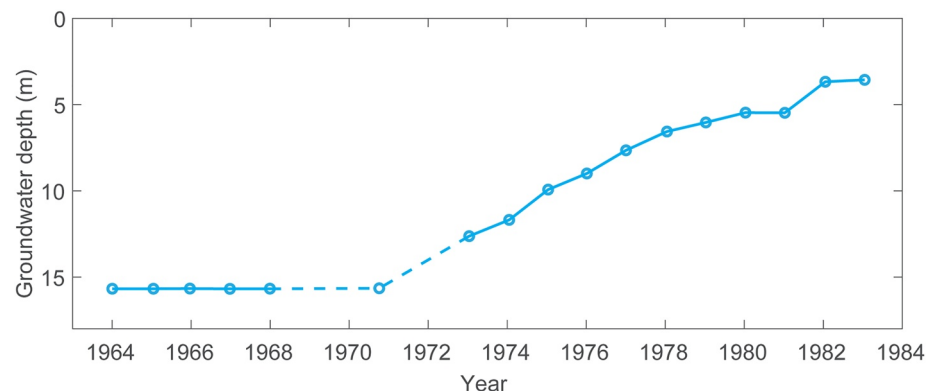


**Figure 13.** Groundwater level changes near the Johnson landslide complex from 1964 to 1984. The dashed lines denote that observations were unavailable and were extrapolated from data observed in adjacent years.

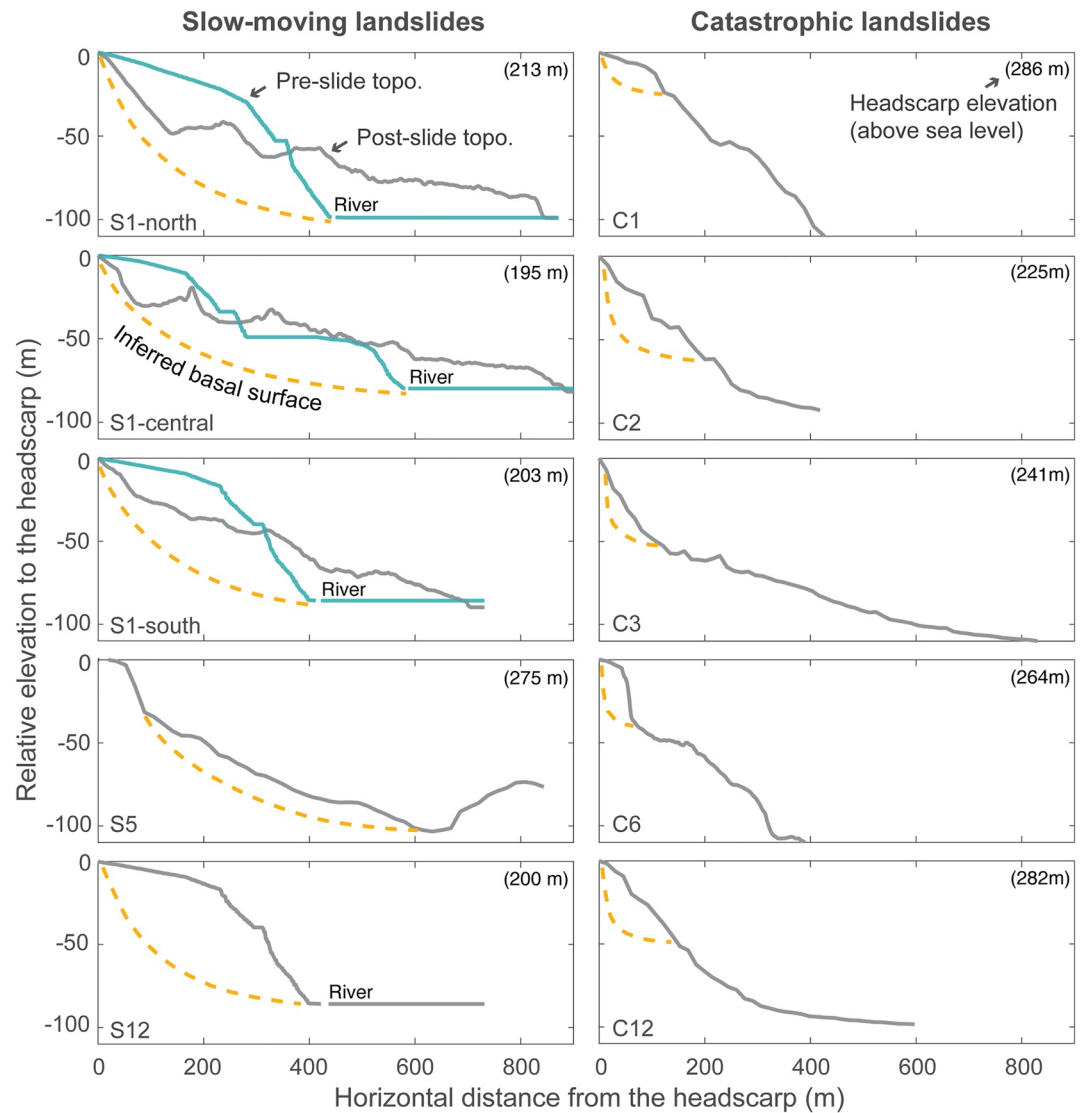


**Figure 14.** Comparison between basal geometry of slow-moving landslides and catastrophic landslides near Hanford. Pre-slide topography of the three transects at landslide complex S1 was obtained from the 1924 U.S. geological survey topographical maps, and the locations of the three-transects are shown in Figure 10 as  $T_1$ – $T_3$ . Post-slide topography of the three transects was from the 2010 lidar DEM. Surface topography of other landslides is obtained from either the 2010 lidar DEM or the National Elevation Datasets (USGS, 2021a, 2021b, 2021c). The basal surfaces of slow-moving landslides were inferred from topographical features, such as dip angle and location of headscarps, internal cracks, and landslide toes. The headscarp location of each landslide was used as the reference point ( $x = 0$ ,  $y = 0$ ) for each panel, and the absolute elevation of the headscarp above sea level was given at the top-right corner of each panel.

## 5. Discussion

### 5.1. Satellite Imagery for Landslide Identification and Monitoring

Satellite imagery has evolved into an effective and efficient tool for identifying and monitoring landslide activity, especially in recent years. High-resolution satellite optical images are widely used for identifying landslides with distinct runout paths, which cause significant surface reflectivity changes (e.g., Xu, George, et al., 2021; Xu, Lu, et al., 2021), whereas radar images are especially sensitive and suitable for detecting and measuring slow-moving landslide motion through radar interferometry processing (e.g., Handwerger et al., 2013; Xu et al., 2020; Zhao et al., 2012). In comparison to conventional field inspection and instrumentation, the global-coverage observation



capability of satellite imagery can significantly enhance the efficiency of landslide monitoring across large spatial scales (e.g., Xu, Schulz, et al., 2021; Zhao et al., 2012).

Ground vegetation and surface modification (e.g., erosion, deposition, and soil moisture change) are the primary factors that cause decorrelation of SAR images, consequently decreasing the accuracy of InSAR measurements for monitoring landslide displacements in a regional scale (e.g., Lu & Kim, 2021; Xu, George, et al., 2021; Xu, Lu, et al., 2021). Such impacts are common in global climate regions abundant in precipitation, such as the Tropical Wet, Tropical Wet and Dry, Mediterranean, Marine West Coast, Humid Subtropical, and Humid Continental climates (Peel et al., 2007). In contrast, InSAR measurements are less affected in Semiarid or Desert climates due to the lack of precipitation and clouds. Consequently, the arid and barren hillslopes near Hanford (see Figure 2b) in this study offer an excellent opportunity to obtain accurate InSAR measurements to characterize the landslide movements. Note that unlike the barren hillslopes, the irrigated farmlands may still experience moderate coherence loss. In addition, the diverse types of landslides that occurred near Hanford, Washington, enabled assessment of other factors such as topography on the dynamics of the landslides through mutual comparisons by naturally excluding the influence of precipitation.

## 5.2. Anthropogenically Induced Landslides and Potential Prevention Measures

Landslides are a natural geomorphic process driven by gravity (Highland & Bobrowsky, 2008); however, recent decades have witnessed increasingly frequent landslide activity resulting from global climate change and expanding anthropogenic activities (Froude & Petley, 2018; Gariano & Guzzetti, 2016). Urban expansion, underground and surface mining, road and reservoir construction, and irrigation farming are typical human activities that have caused numerous landslides worldwide in recent years (Froude & Petley, 2018).

Intensive irrigation farming, which gained increased popularity in semiarid and arid regions since the 1950s, has brought in considerable unexpected landslide issues around the world, along with increased agricultural production (see a review by Garcia-Chevesich et al. (2021)). Widespread landslide activity exacerbate soil erosion and farmland loss, transport sediments to streams harming aquatic lives, and endanger life and property safety of local residents. Stream undercutting of the white bluffs near Hanford is another potential factor to cause slope instability. However, such erosion process is generally gradual and slow compared to the widespread and rapid erosion by irrigation-induced landslides since the 1950s.

In addition, water level change of dammed rivers and reservoirs could impact the waterside landslides in two distinct ways: most landslides reactivated or accelerated in response to water level rise owing to the elevated basal pore pressure (e.g., Kilburn & Petley, 2003; Schuster, 1979; Tang et al., 2019), while a few others accelerated during water table drawdown potentially by the induced seepage force (e.g., Li et al., 2010; Li et al., 2019; Yin et al., 2016). The riverside landslides near Hanford in this study belong to the former category (see Figure 8). Our observed early deceleration phenomenon was not yet reported for the abovementioned reservoir landslides (i.e., Kilburn & Petley, 2003; Schuster, 1979; Tang et al., 2019), possibly due to the unavailability of sufficient monitoring data at those sites. To illustrate, continuous basal pore-pressure measurements are ideally required to identify the early deceleration phenomenon when a landslide is subject to the temporally delayed impacts (i.e., water infiltration and pore-pressure diffusion) of both surface precipitation and reservoir height fluctuations. However, similar early deceleration behaviors were observed for the well-monitored landslides in the French Alps (Van Asch et al., 2007) and New Zealand (Massey et al., 2013).

Considering that anthropogenic activities, such as irrigation farming and reservoir management, could significantly affect slope stability, effective regulations may help to balance the economic development and environmental health. We found in this investigation that the desert landslides near Hanford were primarily triggered by excessive irrigation water that was not fully absorbed by crops and therefore infiltrated into the subsurface layers. Water leakage from unlined canal and wastewater ponds was another major factor that triggered landslides distant from the irrigated farmlands. Consequently, practicing efficient crop irrigation using controlled sprinkler systems is a potential way to save water and reduce irrigation-induced landslides. Furthermore, improved canal lining could be an effective measure to prevent water leakage and therefore the triggered landslides. For dammed rivers and reservoirs, landslide risks could be reduced through careful site selection of reservoirs, slope stabilization measures, and water level management.

### 5.3. Time-Dependent Behaviors of Slow-Moving Landslides

The time-dependent behaviors of slow-moving landslides, such as the observed early deceleration, are often interpreted as controlled by one or multiple of the three possible mechanisms: stress-dependent viscous flow behavior (e.g., Vulliet & Hutter, 1988), rate-dependent shear strengthening (e.g., Sheahan et al., 1996), or forced water circulation (e.g., Baum & Johnson, 1993). We showed in this study that the forced water circulation over irregular basal surface could be a reasonable mechanism to produce adequate resisting force to match the observed velocities for many slow-moving landslides (e.g., Baum & Johnson, 1993; Van Asch et al., 2007). However, we cannot eliminate the possible contributions from the two other mechanisms without sufficient direct evidence, though some studies suggested they might not be able to generate sufficient resisting forces. For example, the stress-dependent viscous flow mechanism required viscosity parameters that were hundredfold higher than the laboratory-tested ones to match the field-measured velocities of a landslide in the French Alps (Van Asch et al., 2007). Rate-dependent shear strengthening usually corresponds to an increase by within 10% per logarithmical cycle of strain rate during undrained triaxial compression tests on clays (Kulhawy & Mayne, 1990; Leroueil, 1996; Sheahan et al., 1996) and therefore, the increases in shear strength for a stably creeping landslide tend to be small. Additionally, worth noting is that the forced water circulation is not a significant factor for fast runout landslides, whose kinetic energy could easily overcome the resistance posed by small bumps (Baum & Johnson, 1993).

The forced water circulation model, which was utilized to simulate the time-dependent behaviors of slow-moving landslides in this study, shares similarities to the models for fault slip and glacier sliding over irregular basal surfaces, yet with distinctly different physical interpretations. Models for glacier sliding primarily involves the stress-dependent regelation process and the rate-dependent viscous flow (e.g., Kamb & LaChapelle, 1964). The fault slip models usually emphasize on elastic deformation between two wavy frictional faults and do not involve the pore-pressure diffusion process (e.g., Chester & Chester, 2000). By comparison, the forced water circulation model assumes a rigid block sliding on an impermeable, wavy surface and focuses on the pore pressure diffusion caused by asymmetrical stress distribution near the basal asperities.

### 5.4. Implications of Basal Geometry Controls on Landslide Dynamics

Landslides initiate from basal shearing failure and may present diverse motion dynamics at the post-initiation stage. Deciphering factors that control landslide post-failure mobility could offer key understanding for mitigating life and property loss from highly mobile landslides. In this study, we found that basal geometry exerts fundamental controls on landslide kinematics in two distinct ways.

First, an irregular basal slip surface could produce significant resistance through forced water circulation to obstruct slow-moving landslides (insignificant for fast-moving ones) after shearing failure initiates on a relatively gentle slope. For slowly advancing landslides, the accumulation of landslide mass above existing terrain that is inherently rough or uneven may result in forced water circulation and a specific signature of motion (e.g., the early deceleration phenomenon). Similar motion signatures were also observed for slow-moving landslides in the French Alps (Van Asch et al., 2007) and New Zealand (Massey et al., 2013). Second, the steepness of basal-topography serves as a critical control on the bifurcation of slow-moving and catastrophic landslides. Steep basal surface and downslope topography are more likely to produce catastrophic landslides due to the rapid kinetic energy gain during the downslope movement. Landslides with steep downslope terrain tend to fail quickly with a short lifecycle because there is insufficient buttressing behavior at the toe to arrest their movement. Landslide blocks breaking apart and forming debris flows under large deformation are another potential factor that enhances landslide mobility. Largely impacted by the slope angle, landslide deposits on a gentle slope from previous catastrophic events could form new slow-moving landslides (Figure 9b).

These fundamental controls on landslide kinematics from basal geometry apply to not only the irrigation-induced landslides, but also many other slow-moving and catastrophic landslides worldwide.

## 6. Conclusions

Landslides in dry climates may be triggered by agricultural irrigation and are a concerning type of anthropogenically induced geohazard. Monitoring the dynamics of these landslides and deciphering their kinematic controls are essential for understanding and reducing their potential hazards. In this investigation, we utilized both satellite

optical and radar imagery to discover both slow-moving and catastrophic landslides from 1996 to 2020 in a Washington desert near Hanford.

We retrieved the time-series displacement of seven slow-moving landslides in the study region using radar interferometry of both ascending and descending Sentinel-1 SAR images between 2015 and 2020. Our analyses reveal that the riverside landslides were triggered by agricultural irrigation yet were strongly regulated by water level variation of the Columbia River where the landslide toes reside. Moreover, the seasonal initiation and cessation of the riverside landslides were not controlled by a constant threshold of river levels, which can be explained by the forced water circulation on an irregular slip surface where accelerated landslide velocity enhances basal resistance and in turn contributes to eventual deceleration of landslide movement prior to a drop in river level. Our numerical simulations show that incorporating the forced water circulation can effectively enhance the prediction accuracy of landslide deceleration time and movement velocity in contrast to using the simple infinite slope assumption. By integrating of satellite observations of two highly similar irrigation-triggered slow-moving landslides, we reveal the life cycle of typical slow-moving landslides in the study region: a rapid acceleration to the peak rate within 3 years followed by slow decelerations with exponentially decreasing rates for about 40 years.

We further investigated how basal geometry could bifurcate the identified slow-moving landslides and catastrophic landslides. By comparing longitudinal topographical profiles of five typical slow-moving landslides and five catastrophic landslides in the study region, we found that steep basal slip surface and runout path are more likely to produce catastrophic landslides with a long runout distance, whereas gentle slip surface and basal slopes at particularly the toe region tend to produce deep-seated, slow-moving landslides.

Our findings could contribute to understanding and mitigation of irrigation-induced landslide around the globe. Moreover, the impacts of basal geometry on landslide post-initiation kinematics are widely applicable to not only irrigation-induced landslides, but also other slow-moving and catastrophic landslides worldwide.

## Data Availability Statement

Historical topographic maps were accessed from the topoView data portal hosted by U.S. Geological Survey (USGS) (<https://ngmdb.usgs.gov/topoview/>). The lidar DEMs were downloaded from the lidarportal hosted by Washington Department of Natural Resources (<https://lidarportal.dnr.wa.gov>). River gauging data of the Columbia River were accessed from the National Water Information System hosted by USGS (<https://water-data.usgs.gov/wa/nwis/>). InSAR time-series measurements that support this study are available online at <https://smu.box.com/v/HanfordDesertSlides>.

## Acknowledgments

We thank William Schulz at U.S. Geological Survey for suggestions on data interpretation and Jinwoo Kim at Southern Methodist University for helping with Sentinel-1 InSAR processing. We also thank Bruce Bjornstad for kindly providing us field photos of multiple landslides near Hanford. This study was funded by NASA Interdisciplinary Research (IDS) in Earth Science Program (80NSSC17K0022) and NASA NISAR Science Team (80NSSC19K1491). Copernicus Sentinel-1 data 2016–2020 were acquired by European Space Agency (ESA) and were accessed from Alaska Satellite Facility (ASF) Distributed Active Archive Center (DAAC).

## References

- Bareither, C. A., Edil, T. B., & Benson, C. H. (2012). Investigation of white bluffs landslides in Washington state. In *GeoCongress 2012: State of the art and practice in geotechnical engineering* (pp. 546–555). <https://doi.org/10.1061/9780784412121.057>
- Baum, R. L., & Johnson, A. M. (1993). Steady movement of landslides in fine-grained soils: A model for sliding over an irregular slip surface. *US Geological Survey Bulletin*, 1842.
- Bennett, D. J., Hubbs, D., & Link, R. A. (2002). *Locke island landslide study white bluffs area Columbia Basin Project*. Report to U.S. Department of the Interior Bureau of Reclamation.
- Bjornstad, B. N. (2006). *Past, present, future erosion at Locke Island (No. PNNL-15941)*. Pacific Northwest National Lab.(PNNL).
- Bjornstad, B. N., & Peterson, R. E. (2019). Hydrogeologic controls and impacts of quaternary landslides along the White Bluffs of the Columbia River, south-central Washington. Retrieved from [https://12c2f97e-e9de-9620-eeb5-c0d53388ee06.filesusr.com/ugd/12afd0\\_7660a9179e4731665eb815ae8ce92c95.pdf](https://12c2f97e-e9de-9620-eeb5-c0d53388ee06.filesusr.com/ugd/12afd0_7660a9179e4731665eb815ae8ce92c95.pdf)
- Casagrande, A. (1976). Liquefaction and cyclic deformation of sands—A critical review. *Harvard Soil Mechanics Series, Harvard University*, 88.
- Chester, F. M., & Chester, J. S. (2000). Stress and deformation along wavy frictional faults. *Journal of Geophysical Research*, 105(B10), 23421–23430. <https://doi.org/10.1029/2000jb900241>
- Chugh, A. K., & Schuster, R. L. (2003). Numerical assessment of Locke island landslide, Columbia River valley, Washington state, USA. In *Proceedings of the 12th pan-American conference on soil mechanics and geotechnical engineering* (pp. 22–26).
- Collin, A. (1846). *Recherches experimentales sur les glissements spontanés des terrains argileux, accompagnées de considerations sur quelques principes de la mecanique terrestre par Alexandre Collin: Texte (Vol. 1)*. Carilian-Goeury et Dalmont. Translation by W.R. Schriever, 1956, *Landslides in clays: Toronto*, University of Toronto Press, 160.
- Costantini, M. (1998). A novel phase unwrapping method based on network programming. *IEEE Transactions on Geoscience and Remote Sensing*, 36, 813–821. <https://doi.org/10.1109/36.673674>
- Cruden, D. M., & Varnes, J. D. (1996). *Landslide types and processes*. Landslides: Investigation and mitigation, transportation research board. National Research Council.

- Drost, B. W., Ebbert, J. C., & Cox, S. E. (1993). *Long-term effects of irrigation with imported water on water levels and water quality*. US Department of the Interior, US Geological Survey.
- Ferretti, A., Savio, G., Barzaghi, R., Borghi, A., Musazzzi, S., Novali, F., et al. (2007). Submillimeter accuracy of InSAR time series: Experimental validation. *IEEE Transactions on Geoscience and Remote Sensing*, 45(5), 1142–1153. <https://doi.org/10.1109/tgrs.2007.894440>
- Froude, M. J., & Petley, D. N. (2018). Global fatal landslide occurrence from 2004 to 2016. *Natural Hazards and Earth System Sciences*, 18, 2161–2181. <https://doi.org/10.5194/nhess-18-2161-2018>
- García-Chevesich, P., Wei, X., Ticona, J., Martínez, G., Zea, J., García, V., & Krahenbuhl, R. (2021). The impact of agricultural irrigation on landslide triggering: A review from Chinese, English, and Spanish literature. *Water*, 13, 10.
- Gariano, S. L., & Guzzetti, F. (2016). Landslides in a changing climate. *Earth-Science Reviews*, 162, 227–252. <https://doi.org/10.1016/j.earscirev.2016.08.011>
- Gould, J. P. (1960). A study of shear failure in certain Tertiary marine sediments. In *Research conference on shear strength of cohesive soils* (pp. 615–641).
- Guerriero, L., Coe, J. A., Revellino, P., Grelle, G., Pinto, F., & Guadagno, F. M. (2014). Influence of slip-surface geometry on earth-flow deformation, Montaguto earth flow, southern Italy. *Geomorphology*, 219, 285–305. <https://doi.org/10.1016/j.geomorph.2014.04.039>
- Handwerger, A. L., Roering, J. J., & Schmidt, D. A. (2013). Controls on the seasonal deformation of slow-moving landslides. *Earth and Planetary Science Letters*, 377, 239–247. <https://doi.org/10.1016/j.epsl.2013.06.047>
- Highland, L., & Bobrowsky, P. T. (2008). *The landslide handbook: A guide to understanding landslides*. US Geological Survey, 129.
- Hutchinson, J. N. (1970). A coastal mudflow on the London clay cliffs at Beltinge, north kent. *Géotechnique*, 20, 412–438. <https://doi.org/10.1680/geot.1970.20.4.412>
- Iverson, R. M. (2000). Landslide triggering by rain infiltration. *Water Resources Research*, 36(7), 1897–1910. <https://doi.org/10.1029/2000wr900090>
- Kamb, B., & LaChapelle, E. (1964). Direct observation of the mechanism of glacier sliding over bedrock. *Journal of Glaciology*, 5(38), 159–172. <https://doi.org/10.3189/s0022143000028756>
- Keefer, D. K., & Johnson, A. M. (1983). *Earth flows: Morphology, mobilization, and movement*. US Geological Survey Professional. Paper 1264.
- Kilburn, C. R., & Petley, D. N. (2003). Forecasting giant, catastrophic slope collapse: Lessons from Vajont, northern Italy. *Geomorphology*, 54(1–2), 21–32. [https://doi.org/10.1016/s0169-555x\(03\)00052-7](https://doi.org/10.1016/s0169-555x(03)00052-7)
- Kulhawy, F. H., & Mayne, P. W. (1990). *Manual on estimating soil properties for foundation design* (No. EPRI-EL-6800). Electric Power Research Inst., Palo Alto, CA (USA); Cornell University, Ithaca, NY (USA). Geotechnical Engineering Group.
- Legros, F. (2002). The mobility of long-runout landslides. *Engineering Geology*, 63, 301–331. [https://doi.org/10.1016/s0013-7952\(01\)00090-4](https://doi.org/10.1016/s0013-7952(01)00090-4)
- Leroueil, S. (1996). Importance of strain rate and temperature effects in geotechnical engineering, measuring and modeling time dependent soil behaviour. *ASCE, GSP*, 61, 1–60.
- Li, D., Yin, K., & Leo, C. (2010). Analysis of Baishuihe landslide influenced by the effects of reservoir water and rainfall. *Environmental Earth Sciences*, 60(4), 677–687. <https://doi.org/10.1007/s12665-009-0206-2>
- Li, S., Xu, Q., Tang, M., Iqbal, J., Liu, J., Zhu, X., et al. (2019). Characterizing the spatial distribution and fundamental controls of landslides in the three gorges reservoir area, China. *Bulletin of Engineering Geology and the Environment*, 78(6), 4275–4290. <https://doi.org/10.1007/s10064-018-1404-5>
- Lu, Z., & Kim, J. W. (2021). A framework for studying hydrology-driven landslide hazards in northwestern US using satellite InSAR, precipitation and soil moisture observations: Early results and future directions. *GeoHazards*, 2, 17–40. <https://doi.org/10.3390/geohazards2020002>
- Mackey, B. H., & Roering, J. J. (2011). Sediment yield, spatial characteristics, and the long-term evolution of active earthflows determined from airborne LiDAR and historical aerial photographs, Eel River, California. *Bulletin*, 123, 1560–1576. <https://doi.org/10.1130/b30306.1>
- Martens, B., Miralles, D. G., Lievens, H., Van Der Schalie, R., De Jeu, R. A., Fernández-Prieto, D., et al. (2017). GLEAM v3: Satellite-based land evaporation and root-zone soil moisture. *Geoscientific Model Development*, 10(5), 1903–1925. <https://doi.org/10.5194/gmd-10-1903-2017>
- Massey, C. I., Petley, D. N., & McSaveney, M. J. (2013). Patterns of movement in reactivated landslides. *Engineering Geology*, 159, 1–19. <https://doi.org/10.1016/j.enggeo.2013.03.011>
- Mizuno, K. (1989). Landsliding of clayey slopes with a wavy slip surface model and its application. *Science Reports of the Institute of Geosciences University of Tsukuba*, (Vol. 10, pp. 87–151).
- Morgenstern, N. R., & Tchalenko, J. S. (1967). Microstructural observations on shear zones from slips in natural clays. *Proceedings of the Geotechnical Conference on Shear Strength Properties of Natural Soils and Rocks*, 1, 147–152.
- Peel, M. C., Finlayson, B. L., & McMahon, T. A. (2007). Updated world map of the Köppen-Geiger climate classification. *Hydrology and Earth System Sciences*, 11, 1633–1644. <https://doi.org/10.5194/hess-11-1633-2007>
- Rice, J. R., & Cleary, M. P. (1976). Some basic stress diffusion solutions for fluid-saturated elastic porous media with compressible constituents. *Review of Geophysics*, 14, 227–241. <https://doi.org/10.1029/rg014i002p00227>
- Rosenthal, D. (1946). The theory of moving sources of heat and its application of metal treatments. *Transactions of ASME*, 68, 849–866.
- Schuster, R. L. (1979). Reservoir-induced landslides. *Bulletin of the International Association of Engineering Geology*, 20(1), 8–15. <https://doi.org/10.1007/bf02591233>
- Schuster, R. L., Chleborad, A. F., & Hays, W. H. (1989). The white bluffs landslides, south-central Washington. In R. W. Glaster (Ed.), *Engineering geology of Washington*, Washington division of geology and earth Resources, Olympia, bulletin (Vol. 78, pp. 911–920).
- Sheahan, T. C., Ladd, C. C., & Germaine, J. T. (1996). Rate-dependent undrained shear behavior of saturated clay. *Journal of Geotechnical Engineering*, 122(2), 99–108. [https://doi.org/10.1061/\(asce\)0733-9410\(1996\)122:2\(99\)](https://doi.org/10.1061/(asce)0733-9410(1996)122:2(99))
- Simoni, A., Ponzá, A., Picotti, V., Berti, M., & Dinelli, E. (2013). Earthflow sediment production and Holocene sediment record in a large Apennine catchment. *Geomorphology*, 188, 42–53. <https://doi.org/10.1016/j.geomorph.2012.12.006>
- Skempton, A. W., & Petley, D. J. (1968). The strength along structural discontinuities in stiff clays. In *Proceedings of the Geotechnical Conference Oslo*, 2, 29–46.
- Spiker, E. C., & Gori, P. (2003). *National landslide hazards mitigation strategy, a framework for loss reduction* (No. 1244). US Geological Survey.
- Stout, M. L. (1971). Slip surface geometry in landslides, southern California and Norway. *Association of Engineering Geologists—Bulletin*, 8, 59–78.
- Tang, H., Wasowski, J., & Juang, C. H. (2019). Geohazards in the Three Gorges reservoir area, China—lessons learned from decades of research. *Engineering Geology*, 261, 105267. <https://doi.org/10.1016/j.enggeo.2019.105267>
- Ter-Stepanian, G. (1965). In-situ determination of the rheological characteristics of soils on slopes. *Proceedings of the International conference on soil mechanics and foundation engineering*, 2, 575–577.
- Terzaghi, K. (1950). Mechanism of landslides. Application of geology to engineering practice (Berkey volume). *Paige, Chairman, Geological Society of America Bulletin*, 83.



- USGS (U.S. Geological Survey). (2021a). National Elevation Datasets –1/3 arc-second DEM. *Ab*, Retrieved from <http://usgs.gov/NationalMap/data>
- USGS (U.S. Geological Survey). (2021b). *National water information system: Web interface*. Retrieved from <https://waterdata.usgs.gov/nwis>
- USGS (U.S. Geological Survey). (2021c). *Mean water velocity for discharge computation at monitoring location 14144700 – Columbia River at Vancouver, WA*. Retrieved from <https://waterdata.usgs.gov/nwis/uv?14144700>
- Van Asch, T. W., Van Beek, L. P. H., & Bogaard, T. A. (2007). Problems in predicting the mobility of slow-moving landslides. *Engineering Geology*, 91, 46–55. <https://doi.org/10.1016/j.enggeo.2006.12.012>
- Vulliet, L., & Hutter, K. (1988). Viscous-type sliding laws for landslides. *Canadian Geotechnical Journal*, 25(3), 467–477. <https://doi.org/10.1139/t88-052>
- WRCC (Western Regional Climate Center). (2021). *Remote automatic weather stations*.
- Xu, Y., George, D. L., Kim, J., Lu, Z., Riley, M., Griffin, T., & de la Fuente, J. (2021). Landslide monitoring and runout hazard assessment by integrating multi-source remote sensing and numerical models: An application to the gold basin landslide complex, northern Washington. *Landslides*, 18, 1131–1141. <https://doi.org/10.1007/s10346-020-01533-0>
- Xu, Y., Kim, J., George, D. L., & Lu, Z. (2019). Characterizing seasonally rainfall-driven movement of a translational landslide using SAR imagery and SMAP soil moisture. *Remote Sensing*, 11(20), 2347. <https://doi.org/10.3390/rs11202347>
- Xu, Y., Lu, Z., & Kim, J. W. (2021). P-band InSAR for geohazard detection over forested terrains: Preliminary results. *Remote Sensing*, 13(22), 4575. <https://doi.org/10.3390/rs13224575>
- Xu, Y., Lu, Z., Schulz, W. H., & Kim, J. (2020). Twelve-year dynamics and rainfall thresholds for alternating creep and rapid movement of the Hooskanaden landslide from integrating InSAR, pixel offset tracking, and borehole and hydrological measurements. *Journal of Geophysical Research: Earth Surface*, 125, e2020JF005640. <https://doi.org/10.1029/2020jf005640>
- Xu, Y., Schulz, H. W., Lu, Z., Kim, J. W., & Baxstrom, K. (2021). Geologic controls of slow-moving landslides near the U.S. West Coast. *Landslides*, 18, 3353–3365. <https://doi.org/10.1007/s10346-021-01732-3>
- Yin, Y., Huang, B., Wang, W., Wei, Y., Ma, X., Ma, F., & Zhao, C. (2016). Reservoir-induced landslides and risk control in three gorges Project on Yangtze river, China. *Journal of Rock Mechanics and Geotechnical Engineering*, 8(5), 577–595. <https://doi.org/10.1016/j.jrmge.2016.08.001>
- Zaruba, Q., & Mencl, V. (1982). *Landslides and their control*, Elsevier.
- Zhao, C., Lu, Z., Zhang, Q., & de La Fuente, J. (2012). Large-area landslide detection and monitoring with ALOS/PALSAR imagery data over northern California and southern Oregon, USA. *Remote Sensing of Environment*, 124, 348–359. <https://doi.org/10.1016/j.rse.2012.05.025>